GC
7.8
.R32
1996

A Characterization of Internal Solitons in the SWARM Region of the New York Bight

MARINE
BIOLOGICAL
LABORATORY
LIBRARY
WOODS HOLE, MASS.
W. H. O. I.

by

Brian Scott Racine

B.S. Millersville University
(1991)

Submitted in partial fulfillment of the
requirements for the degree of

MASTER OF SCIENCE

at the

MASSACHUSETTS INSTITUTE OF TECHNOLOGY

and the

WOODS HOLE OCEANOGRAPHIC INSTITUTION

August 1996

© Brian Scott Racine 1996

The author hereby grants to MIT and to WHOI permission to reproduce
and to distribute copies of this thesis document in whole or in part.

Signature of Author .....
Joint Program in Physical Oceanography
Massachusetts Institute of Technology
Woods Hole Oceanographic Institution
August 9, 1996

Certified by .....
Robert C. Beardsley
Senior Scientist
Thesis supervisor

Accepted by .....
Paola Rizzoli
Chair, Joint Committee for Physical Oceanography
Massachusetts Institute of Technology
Woods Hole Oceanographic Institution

WHOI Gift 1997

A CHARACTERIZATION OF INTERNAL SOLITONS IN THE SWARM REGION OF THE NEW YORK BIGHT

by

Brian Scott Racine

Submitted in partial fulfillment of the requirements for the degree of
Master of Science at the Massachusetts Institute of Technology
and the Woods Hole Oceanographic Institution
August 24, 1996

Abstract

A field experiment was undertaken during July and August of 1995 aimed at understanding the interaction of acoustic signals with the internal wave field off the coast of New Jersey. As part of SWARM (Shallow Water Acoustics in a Random Medium), physical data were collected in 75 m of water near 39° 15.34′ N, 72° 56.59′ W with three thermistor strings, a bottom-mounted ADCP, and yo-yo CTDs. These data spanned a two-week period of the month-long study. With the exception of a time following a storm event, during which the generation mechanism near the shelf break was effectively switched off, large-amplitude (up to 20 meters), rank-ordered groups of internal solitons were observed traveling through the region approximately every 12.4 hours. These groups of solitons progressed across the shelf with phase speeds of 61.8 ± 14.9 cm/s with a heading of 280 ± 31° T. Two-layer finite-depth theory was tested on this data and shown to consistently overpredict the phase speed of the internal solitons within each group. Predictions of horizontal scale, particle velocities, and displacements were in qualitative agreement with two-layer finite-depth dynamics.

Acknowledgments

For boundless enthusiasm and scientific advice, I would like to thank my academic co-advisors Bob Beardsley and Jim Irish, as well as Jim Lynch (a.k.a. SWARM guru). Without their encouragement and continued support, the completion of this thesis would have never come about. A special thanks to Jim Irish for the invaluable experience I gained as a research scientist aboard the many GLOBEC deployment and recovery cruises - sometimes romantic, never glamorous, but always a lot of fun.

For their enduring friendship and invaluable behind-the-scenes support, my thanks goes out to Derek Fong and Lyn Harris. Although computer codes and UNIX tutorials made my work as a graduate student a bit easier, my life is much richer and my horizons a bit broader for having met you. To my other friends, Jay Austin, Natalia Beliakova, Melissa Bowen, François Primeau, Jamie Pringle, Miles Sundermeyer, Nicole Suoja, Sandra Werner, and Bill Williams, all I can think to say is thanks gang and remember to invite me to bridge games and barbecues once in a while.

In keeping with tradition, I have saved the most important people in my life for last. It is impossible to convey the emotions that writing this paragraph stirs in me. To Kate, an eternity of thanks can never repay the debt of gratitude I feel I owe you. For being my closest friend, my stiffest competition, my most ardent supporter, my ally in all things important and whimsical, for moving to Massachusetts with me, then to Maine, then back to Massachusetts, for understanding and providing me the courage to live my life to its fullest even through impossible odds, for giving me the most beautiful son a father could dream of - for all these things, I love you. To Bob, the last nine months of my life have seen incredible changes in the person I am becoming. For those changes I have you to thank. For being the person you are and showing me new ways to view people and the world, I have you to admire. For being my partner in life and standing by me even when I make it next to impossible, I have you to love. I only hope the rest of our life together continues to grow and strengthen the way it has so far.

Support for this work was provided by a National Science Foundation grant OCE - 9313670.

Contents

List of Figures

List of Tables

Chapter 1

Introduction

1.1 Related History

When one begins to look at the origin of our current understanding of internal waves and the more unusual internal soliton, one quickly realizes that even without the sophistication of twentieth-century science, humans have been aware of these phenomena for a long time. *Ekman* [1904] pointed out that there were reports made in Roman times of "sticky water" and that Viking peoples certainly recognized the surface manifestations of internal solitons in the many fjords of what is now northern Europe. A very elegant description of many of the salient features of solitary waves was first written down by *Russell* [1838]:

> I was observing the motion of a boat which was rapidly drawn along a narrow channel by a pair of horses, when the boat suddenly stopped - not so the mass of water in the channel which it had put in motion; it accumulated round the prow of the vessel in a state of violent agitation, then suddenly leaving it behind, rolled forward with great velocity, assuming the form of a large solitary elevation, a rounded, smooth and well-defined heap of water, which continued its course along the channel apparently without change of form or diminution of speed. I followed it on horseback, and overtook it still rolling on at a rate of some eight or nine miles an hour, preserving its figure some thirty feet long and a foot to a foot and a half in height. Its height gradually diminished and after a chase of one or two miles I lost it in the windings of the channel. Such, in the month of August, 1834, was my first interview with that singular and beautiful phenomenon.

Although this was his first encounter with such a wave, Russell was almost prophetic in his choice of words in characterizing what he had seen. Traits such as unchanging form and rapid velocity, isolated, solitary, and gradual amplitude reduction are all common to our modern understanding of internal solitons in the coastal ocean.

It was not until sixty years later that a theoretical framework for describing these waves was built by *D.J. Korteweg* and *G. De Vries* [1895]. In their work, *Korteweg* and *De Vries* approximated the Navier-Stokes equations with a balance between the nonlinear terms and the dispersive terms, with the solution being a stable isolated feature known as a solitary wave (a more complete description of which will appear in Chapter 2). Again it seemed like a new field of research would develop in the wake of this discovery. However, for another seventy years, the solitary wave solution that had been discovered remained little more than a mathematical construct. It was not until *Zabusky* and *Kruskal* [1965] reported that these solitary waves retained both their shapes and velocities under collision in a computer model that they had developed, that people again began to have interest in what had been termed a "soliton". Much like the terms proton and neutron, the soliton was so named because its behavior seemed to posses qualities of elementary particles, and as quantum physics has taught us, the line between wave and particle is not always so clearly drawn.

To accompany the interest generated by the model results, satellite oceanography was beginning to contribute images of surface features in regions of the New York Bight in the early 1970's which bore remarkable resemblance to the "surface slicks" described by *Russell* and others [*Apel et al.*, 1975a]. Satellites such as ERTS (Earth Resources Technology Satellite) used instruments like the multispectral scanner (MSS) to detect these slicks and show that they were phase-locked with the semidiurnal tide [*Zheng et al.*, 1993]. Not only did this give valuable indications about where one might expect to find internal solitary waves, but it also suggested a generation mechanism - the motion of the barotropic tide over the shelf break. Due to the fact that satellite images provide no information about vertical structure, an experiment was devised (NYBERSEX - New York to Bermuda Remote Sensing Experiment) in 1974 to simultaneously measure horizontal and vertical fields which could pin down the identity of these phenomena. The result of this effort was to verify that the subsurface structure associated with the surface slicks was indeed consistent with internal wave theory [*Apel et al.*, 1975b].

In 1975 and 1976, Exxon attempted to begin offshore drilling operations in the Andaman Sea off the coast of Thailand. Much to their dismay, Exxon scientists aboard the drillship Discover 534 noticed that they were unable to securely mount drilling operations to the ocean floor (600 to 1100 meters below) because each time they tried, the machinery was lifted and pushed away from the site by some "mysterious phenomenon" [*Osborne et al.*, 1978]. As large-amplitude internal waves seemed to be a likely explanation, an experiment was conducted to measure internal waves and the response of the drillship as they passed beneath. The study showed rank-ordered groups of internal solitons which passed through the region about every 12 hours and possessed amplitudes on the order of 10 meters with speeds of 4 knots or more [*Osborne* and *Burch*, 1980]. The presence of these enormous waves in the southwestern Pacific has since been well-documented by both satellites and field studies. While the internal waves and solitons observed in the New York Bight are not as energetic, they do occur in regions of interesting frontal dynamics and high primary productivity. As a result, understanding the role they play on the northeast US coast is crucial to our understanding of the coastal environment.

1.2 SWARM

From July 20 to August 12, 1995, an experiment designed to study shallow water acoustics in a random medium (SWARM) was undertaken off the coast of New Jersey in the New York Bight (NYB). The timing and region were chosen for the following reasons. First, during that portion of the year, the thermocline is fully developed and has little or no chance of being eroded due to surface cooling and/or mixing events. Second, due to the work of Apel and others, that region of the New York Bight was known to support energetic internal soliton generation. As a result, the planners were confident that there would be no shortage of internal soliton events during SWARM. The goal of SWARM was to study the effects heterogeneity of the water column and ocean floor could have on acoustic signals in the 50 - 700 Hz range. This required the use of three oceanographic research vessels (*R/V Endeavor*, *R/V Oceanus*, and *R/V Cape Hatteras*) and nearly thirty moorings deployed along a seventy-kilometer path across the shelf. The depth range of this track was 30 meters to 120 meters. Since internal solitons may

strongly influence acoustic propagation, much of the sampling was done quickly enough to resolve these relatively high-frequency events.

The *R/V Endeavor* and the *R/V Oceanus* were responsible for deployment and recovery of moored instrumentation, collection of background information from CTD profiles and ship-mounted ADCPs, and meteorological monitoring. While the *R/V Oceanus* remained at anchor to receive acoustic transmissions and make more than 160 yo-yo CTD casts, the *R/V Endeavor* conducted underway sampling, including expendable bathythermograph (XBT) surveys, multiple tow-yo CTD profiles along the transmission path, chirp sonar, and radar imaging. From July 31 to August 5, the *R/V Cape Hatteras* was responsible for signal projection as well as the collection of backscatter data. These data were used to aid in the imaging of the internal wave field.

In this thesis, I will focus on analysis of measurements made near the 75-m isobath with a directional array of thermistor chains and one bottom-mounted ADCP. Eleven thermistors, ranging in depth from 17.5 meters to 57.5 meters, with fairly regular spacing, recorded data each minute. A narrow-band RDI 300 kHz ADCP was moored about a kilometer from the thermistor array. The ADCP was set to transmit 225 pings per ensemble, with an ensemble averaging interval of 90 seconds. The unit was bottom-mounted with four upward-looking beams oriented 30° from the vertical. The return signal was averaged over 4 meter bins, and horizontal velocities accurate to within approximately 1 cm/s were recorded. The quality of the ADCP data was excellent with the exception of the near-surface zone where side-lobe reflection effects became more pronounced. Information on the deployment, depth, and location of each of these instruments is summarized in Table 1. In addition, high-quality supporting data (especially CTD profile data) were collected in SWARM that will be examined to help interpret the moored data.

Instrument	Latitude	Longitude	Depth	Dates
T-String 598	39° 15.75' N	72° 57.31' W	73 m	7/28/95 - 8/9/95
T-String 307	39° 15.41' N	72° 57.27' W	74 m	7/28/95 - 8/9/95
T-String 309	39° 15.82' N	72° 56.76' W	73 m	7/28/95 - 8/9/95
ADCP I212	39° 15.34' N	72° 56.59' W	75 m	7/28/95 - 8/9/95

Table 1.1: Description of instruments used for the characterization of the soliton field.

The goal of this thesis is to characterize the internal solitons observed during SWARM. In subsequent chapters, I will revisit the theoretical framework for internal solitons, describe the observations in this context, and summarize the results of this research.

Chapter 2

Theoretical Framework

2.1 KdV Equations

Near the turn of the century, *Korteweg* and *de Vries* [1895] were working on an analytical solution to the Navier-Stokes equations for long gravity waves in a channel. They found that when the nonlinear and the dispersive terms balance, isolated solitary waves comprise a solution. The equation that they studied was written as

$$\eta_t + c_o\eta_x + \alpha\eta\eta_x + \gamma\eta_{xxx} = 0,$$

where

$$c_o = \sqrt{(gh)},$$
$$\alpha = 3c_o/2h,$$
$$\gamma = c_o h^2.$$

In this equation, $\eta = \eta(x,t)$ is the surface displacement associated with the soliton amplitude, x is the along-track distance, h is the depth of the fluid, and c_o is the associated linear phase speed in the x direction. If the balance described above holds, the solution to this equation is

$$\eta(x,t) = \eta_0 \, \mathrm{sech}^2[(x - ct)/L],$$

where

$$c = c_o \, (1 + \eta_o/2h),$$
$$L = \sqrt{(4h^3/3\eta_o)}.$$

In these expressions, η_o is the maximum displacement and c is the actual phase speed. L is the characteristic horizontal length scale for the solitary wave and depends inversely on the wave amplitude [*Osborne* and *Burch*, 1980]. The shape of this solution is a single elevation (Figure 2.1).

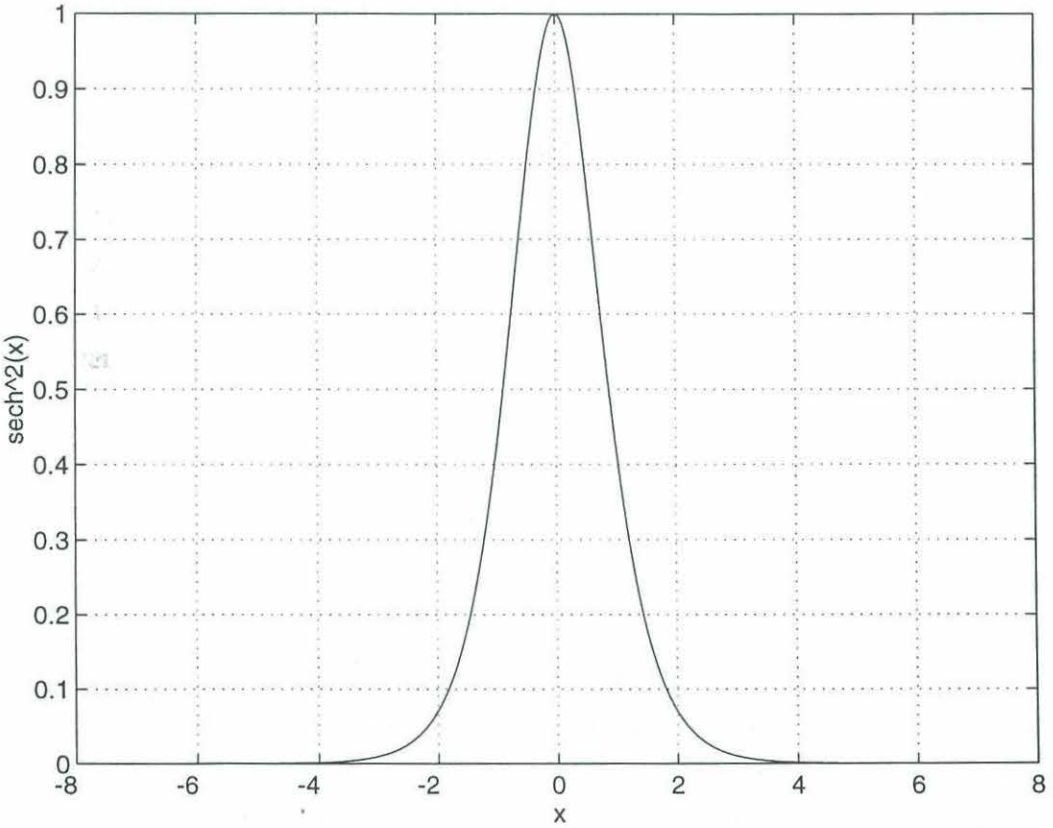

Figure 2.1: General shape of solitary waves of elevation.

In a stratified fluid, solitons are internal waves which propagate along the main pycnocline rather than on the surface (as described by the channel solution above). A

vertical profile of density during SWARM looks fairly constant in the upper 25 meters, followed by a sharp pycnocline between 20 and 35 meters and slowly varying density in the bottom 40 meters. As a result, although not a perfect two-layer system, we might expect that much of the dynamics is explained by this simplified system. In the discussion that follows, the upper layer will be of density ρ_1 and depth h_1, while the lower layer density and depth will be ρ_2 and h_2, where $h_1 < h_2$. In this situation, the solution for $\eta(x,t)$ has exactly the same form except that the solution parameters are now a function of this idealized stratification. When $h_1 < h_2$ and the horizontal scale L is large compared to the total water depth, the soliton exists as a wave of depression rather than elevation and a minus sign appears [*Osborne* and *Burch*, 1980]

$$\eta(x,t) = -\eta_0 \, \mathrm{sech}^2[(x - ct)/L],$$

where

$$c_o = [\, g(\Delta\rho/\rho)h_1/(1 + r)]^{1/2},$$
$$\alpha = -(3c_o/2)[(1 - r)/h_1],$$
$$\gamma = c_o h_1 h_2/6,$$

with

$$\Delta\rho = \rho_2 - \rho_1,$$
$$r = h_1/h_2,$$
$$c = c_o(1 - \eta_0\alpha/3\, c_o),$$
$$L = (-12\gamma/\eta_o\alpha)^{1/2}.$$

For the case of $h_1 < h_2$, the internal soliton can only exist as a wave of depression, so that solitons can only be generated from an initial waveform that has a downward displacement. Internal waveforms that have positive displacements can not generate solitons in this situation. Another method of generating internal solitons, as discussed by *Joseph* [1977] and *Djordjevic* and *Redekopp* [1978], involves a process called fissioning. Fissioning is the process by which an initial solitary wave breaks into a packet of smaller internal solitons as it propagates into shallower water (provided h_1

remains less than h_2). It can also be shown that the number of solitons that can be generated in these so-called rank-ordered groups is given by

$$N \leq [(32/3)(h_1/h_{2s})(1 - h_1/h_{2s})/(\eta_0/h_1)]^{1/2} \ln[(6/\pi)(\eta_o/h_1)(h_{2\infty}/h_1)]$$

where h_{2s} is the lower layer thickness in the shallower water and $h_{2\infty}$ is the layer thickness in the deeper generation zone. In other words, generation may occur in one of at least two ways - initial wave evolution in constant depth, or fissioning as an initially stable solitary wave progresses into shallower water. It is the latter that this thesis will most closely examine and which will be more clearly described in the following section of this chapter.

2.2 A Physical Description of The Generation Process

Conventional wisdom suggests that the necessary conditions for internal soliton generation are the following: an energetic barotropic tide, a time during which the Froude number is supercritical ($v/c > 1$, where v is the fluid velocity and c is the phase speed), ambient stratification, and rapidly changing topography [*Baines* 1973, 1974, 1982, and *Hibiya* 1986, 1988].

To understand how these factors contribute to the generation of internal solitons propagating shoreward from the shelf break, let us consider a region in the vicinity of the shelf break in which the water column has some ambient stratification and a near-surface pycnocline (Figure 2.2). In this region the semidiurnal tide can force periodic currents which may be in excess of 50 cm/s during the flood and ebb, and whose principal axes define an ellipse that is oriented perpendicular to the isobaths (as found in the NYB) [*Moody et al.*, 1984]. Let us further assume we are at the slack tide before the ebb. As the ebb begins, a column of water is moved from the shelf into a deeper region over the shelf break. If we imagine the isopycnals to be initially flat, as the column is moved into deeper water, they must be depressed due to continuity. The energy stored in the forming depression is radiated away in both off and onshore directions in the form of small amplitude internal waves. Let us restrict our continuing

explanation to a two-dimensional slice in the cross-isobath direction. As the ebb continues to strengthen, the waves propagating offshore continue to do so unhindered. However, since the tidal velocity has begun to increase beyond the speed at which internal waves can travel toward shore (supercritical Froude number), the waves begin to pile up in that region. As a result, the amplitude of the net disturbance also continues to grow. During this time, the internal waves that have piled up have the opportunity to interact nonlinearly. As the ebb begins to weaken, the tidal velocity in the offshore direction lessens to a point where it is matched by the phase speed of the now sizable disturbance (often called a lee wave). At that time, the disturbance begins to move toward shore. As the tide starts to shift from ebb to flood, the initial depression evolves into a large solitary wave which then fissions into a rank-ordered group of solitons. During the flood, one might at first expect the same mechanism to generate a solitary wave that would then travel into deeper water. However, due to the fact that tidal velocities in the deeper region are never large enough to cause the build-up of waves, no such disturbance is generated.

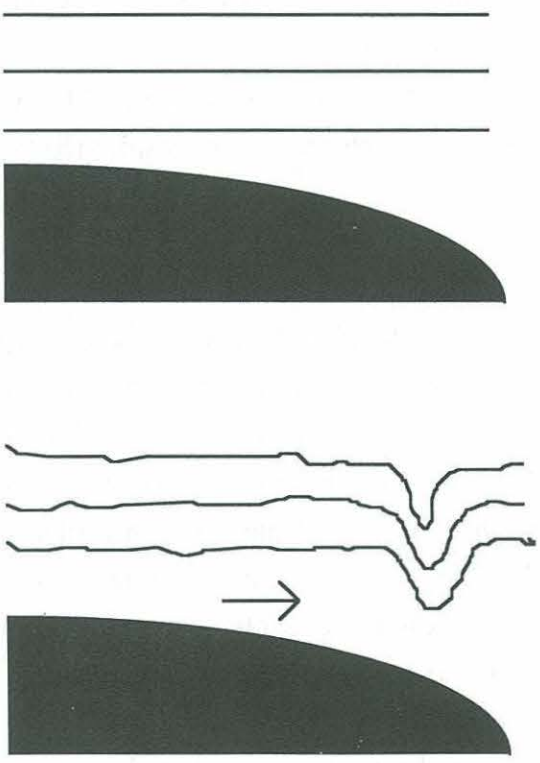

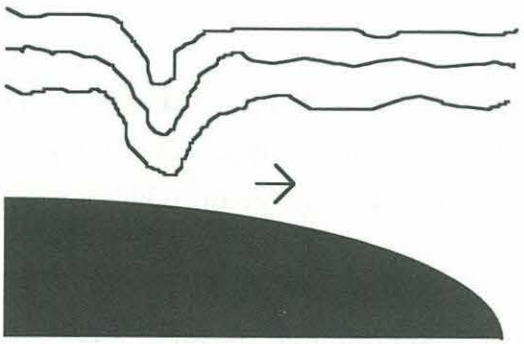

Figure 2.2: Vignettes portraying the ebb portion of the soliton generation cycle.

2.3 Theoretical Predictions

Internal soliton solutions can be found in a two-layer fluid in the following three basic regimes:

(1) Deep-water theory [*Benjamin*, 1967; *Ono*, 1975]:

$$L/H \rightarrow 0,\ L/h_1 >> 1,\ \eta_o/\ h_1^2 \sim O(1)$$

(2) Finite-depth theory [*Joseph*, 1977; *Kubota et al.*, 1978]:

$$L/\ h_1 >> 1,\ h_1/H << 1,\ L/H \sim O(1),\ \eta_o L/\ h_1^2 \sim O(1)$$

(3) Shallow-water theory [*Benjamin*, 1966; *Benney*, 1966]:

$$L/H >> 1,\ h_1/H \sim O(1),\ \eta_o L^2/H^3 \sim O(1)$$

where $H = h_1 + h_2$ is the water depth, L is the half-amplitude length, and η_o is the maximum amplitude of the soliton. During SWARM, we found L = 100 m, H = 75 m, h_1 = 22 m, and η_o = 10 m, so that

$$L/\ h_1 = 4.55,\ \ h_1/H = 0.29,\ \ L/H = 1.33,$$
$$\eta_o L/\ h_1^2 = 2.07, \text{ and } \eta_o L^2/H^3 = 0.24.$$

Although the shallow-water two-layer dynamics (discussed in section 2.1) would be the least cumbersome model, these values suggest that finite-depth theory is the more appropriate context within which to evaluate the data.

Finite-depth KdV theory predicts several quantities that one might consider examining [*Zheng et al,* 1993]. For example, the phase speed of the individual solitons in each rank-ordered group might be investigated to see if nonlinearity has increased the value above the linear wave theory prediction. That is, the nonlinear phase speed is given by

$$c = c_o \{1 + h_1/2H [1 + H/b (1 - a^2b^2)]\},$$

where

$$c_o = [g (\Delta\rho/\rho) (h_1h_2/H)]^{1/2},$$
$$b = 4h_1^2/3\eta_o,$$
$$\tan(aH) = 1/(ab).$$

The typical values for these parameters during SWARM was η_o = 5 m, $\Delta\rho$ = 4.8 kg/m^3, ρ = 1021.2 kg/m^3, h_1 = 22 m, h_2 = 53 m, and H = 75 m. This yields an estimate for the linear phase speed of c_o = 86 cm/s. It should be noted that this way of estimating the linear phase speed will overpredict the actual value. The reason for this overprediction is that the system is not perfectly two-layered. Ambient stratification with a finite-thickness pycnocline effectively slows the propagation of the solitons from that predicted by two-layer shallow-water theory. The nonlinear phase speed estimates will be checked for a typical group of rank-ordered solitons in Chapter 4.

In addition, the interface displacement is given by

$$\eta(x,t) = -\eta_o/\{\cosh^2[a(x-ct)] + \sinh^2[a(x-ct)]/(a^2b^2)\}.$$

For typical values of a and b during SWARM, the $\sinh^2[a(x-ct)]/(a^2b^2)$ is small in comparison to $\cosh^2[a(x-ct)]$, and to lowest order the profile is identical to shallow-water theory.

Also, there exist unique solutions for the particle velocities in the upper and lower layers of the water column [*Phillips*, 1966].

In the upper layer,

$$u_1(x,t) = -(c_o/h_1)\,\eta(x,t),$$

while in the lower layer,

$$u_2(x,z,t) = (c_o k)\,\{\cosh[k(H + z)]/\sinh(kh_2)\}\,\eta(x,t).$$

From these expressions, it is clear that the amplitude of the horizontal velocity in the upper layer does not change with depth, while in the lower layer it does. Another difference to be noted is that the velocities are of opposite sign. As a consequence, in the vicinity of the layer change, the velocity rapidly changes direction. In reality, one might expect to see no horizontal velocity at all in that region - an unusual but viable way to track the vertical position of the pycnocline. It is important to note that while looking at the actual data, the background current structure needs to be effectively removed to observe this effect. Otherwise, the baroclinicity of the ambient flow could contaminate the observations. A full discussion of how this is accomplished will accompany Chapter 3.

Theory suggests several important predictions for soliton displacements. The most obvious is that the shape of such a wave should agree qualitatively with the $\mathrm{sech}^2(x,t)$ solution predicted by both KdV and finite-depth theory. A sinusoidal wave train is certainly a different phenomenon than a single isolated packet of solitons. Also, the fact that the upper layer thickness is smaller than the lower layer thickness ($h_1/h_2 <$

1) implies that these solitons exist as waves of depression - they can not exist as an upward bulge in the pycnocline. Although we are conceptualizing this problem as a two-layer system, the fact remains that there is some stratification in the rest of the water column. As a result, the temperature data should exhibit non-zero vertical displacements everywhere, not just at the layer interface. Therefore, we expect to see large vertical displacements near the depth where the horizontal particle velocities change signs, with decaying magnitudes both above and below that depth. This effect is consistent with the fact that vertical velocities are also largest in the pycnocline region and decay away from it.

Chapter 3

The Physical Setting

The physical setting of any field experiment needs to be described in order to have a better intuitive grasp of the analysis of the data. This thesis uses data collected near the 75-m isobath by shipboard measurements on the *R/V Oceanus*, moored thermistors, and a bottom-mounted ADCP. Temperature, salinity, and density will be described using the CTD yo-yo casts conducted throughout the experiment. In order to describe the advective background field more effectively, the low-pass filtered temperature data from the thermistor strings will also be shown. The bottom-mounted ADCP was employed in the characterization of the currents, including their time evolution, magnitudes, principal forcing frequencies, and response to meteorology.

While many of the SWARM researchers were concerned with the range-dependent properties of these fields, I limited myself to the region close to the thermistor antenna and ADCP. In so doing, the analysis required looking at how the soliton signature changed as a function of time at a single position, and what might be responsible for that change. A large storm event brought anomalous winds and currents to the region for a period near the end of the experiment. During this event, the background fields changed, and the generation mechanism responsible for soliton production was effectively switched off. The latter effect will be more carefully described in Section 3.3.

Along the SWARM line, the temperature and salinity records showed some of the well-documented features associated with the Mid-Atlantic Bight (MAB). At the shelf break, the clearest feature was the so-called "cold pool" of relatively fresh shelf water. The characteristics of this water mass were temperatures ranging from 7 - 12° C and salinities of 32.0 - 33.5 ppt. This was visible at both the 75-m site and closer to the shelf break. Moving off the shelf, the influence of the Gulf Stream was felt in both temperature and salinity with ranges of 12 - 20° C and 33.5 - 35.5 ppt.

3.1 Temperature

In considering the time series that the thermistor strings provided, there are several ways one might consider trying to unravel the signal into something which can be easily understood. One could simply contour the full recorded signal in all of its complexity, or alternatively, the signal could be separated into its constituent time scales. The latter approach allows us to look at the advective time scale (low-pass filtered), the soliton time scale (high-pass filtered), as well as the tidal time scale (extracted by harmonic analysis). In so doing, the full record can be thought of as a sum of all of these parts. This allows a clearer grasp of what is seen in each regime. The advective regime was obtained using a 36-hour Lanczos low-pass filter. It shows the background evolution of temperature as a function of depth during SWARM (Figure 3.1). No attempt has been made to explain the various features present in this record due to the fact that neither the meteorological forcing nor the baroclinic eddy field over the shelf were examined.

Superimposed on the advective background is the internal soliton field. To produce time series which contained these high-frequency bursts of energy, a high-pass Butterworth filter was used. Contouring these time series for each of the three T-strings allowed me to determine the timing and directionality of the internal solitons. It is instructive to look at this regime for all three of the T-strings for subsections of the entire record at the same time. That way, the reader can begin to appreciate both the complexity and periodicity of the signal. This requires a fairly large number of figures, which are presented in Appendix A.

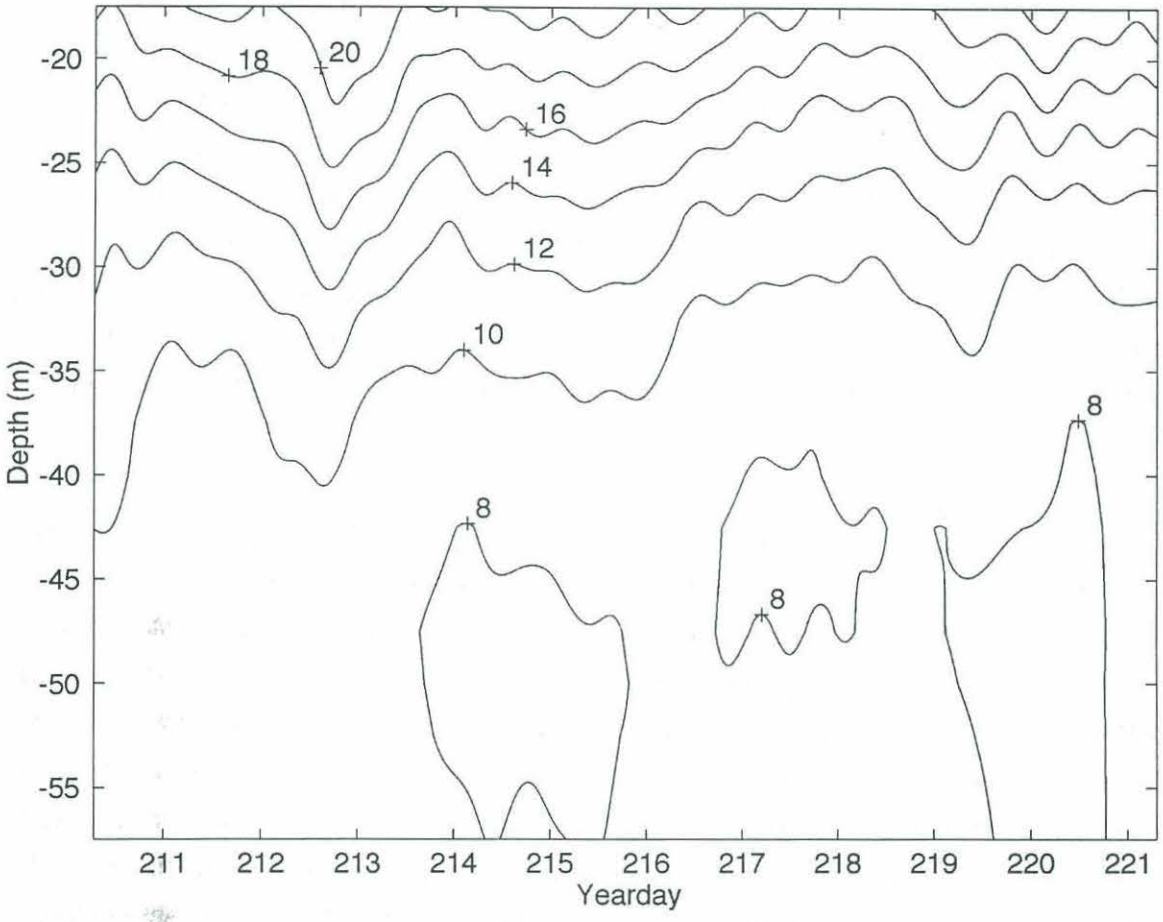

Figure 3.1: Contour of Lanczos filtered T-string 598 time series (cutoff pd. = 36 hours).

Several key points need to be noted in looking at the time series in Appendix A. First of all, the soliton groups arrive with periodicity of approximately 12.4 hours and as such agree with the predictions of the lee wave generation mechanism. That is, they are generated by the M2 tidal current and as a result are phase locked to it. Second, within each of the envelopes associated with the solitons, what is typically seen is not the simple rank-ordered group. Instead, a fairly complex set of undulations is observed which is a result of the fact that several rank-ordered groups arrive at the T-string antenna simultaneously. Although passing through each other theoretically generates little more than a phase shift in solitons, if they are overlapping as they pass the instruments, the observed signal in temperature and velocity is the sum of the individual signals. The majority of the bursts were exactly this way which represented much of the

difficulty in distinguishing individual members for characterization purposes. The last impacting feature I alluded to earlier - the effect of the large wind event on August 7. If one compares the soliton field from before this event with the time during and immediately following it, there is a clear change in the number and character of the solitons. For example, during the period from yeardays 209.8 to 213.8, the energy bursts are very organized and their envelopes appear about twice a day. From yearday 213.8 through 218.8 the rank-ordered groups are still present with the correct periodicity, however their character is much less organized and distinct. After yearday 218.8 (August 6), the observation of soliton groups ceases due to the shutting off of the generation mechanism described previously. Due to the fact that this phenomenon is best described in terms of currents, further explanation is reserved for Section 3.3.

The CTD casts provide a sense of the stratification that supports the internal soliton field. A total of 165 yo-yo casts were completed during the nearly two weeks of active data collection. A superposition of these casts including the mean field is presented in Figure 3.2. In this figure, we see a shallow surface mixed layer of about 2-m to10-m depth. The surface temperature within the mixed layer varied from 23° C to 27° C during SWARM. The thermocline was located in the 10-m to 30-m range, with a mean temperature that dropped from 26° C to less than 10° C. Beneath the thermocline, an intermediate layer of cold water occurred with temperature less than 10° C. This temperature-minimum layer represents the "cold pool" water at the site. The increase in temperature near the bottom is offset by a corresponding increase in salinity, keeping the water column gravitationally stable. This warm bottom layer reflects water from the base of the shelf-slope front.

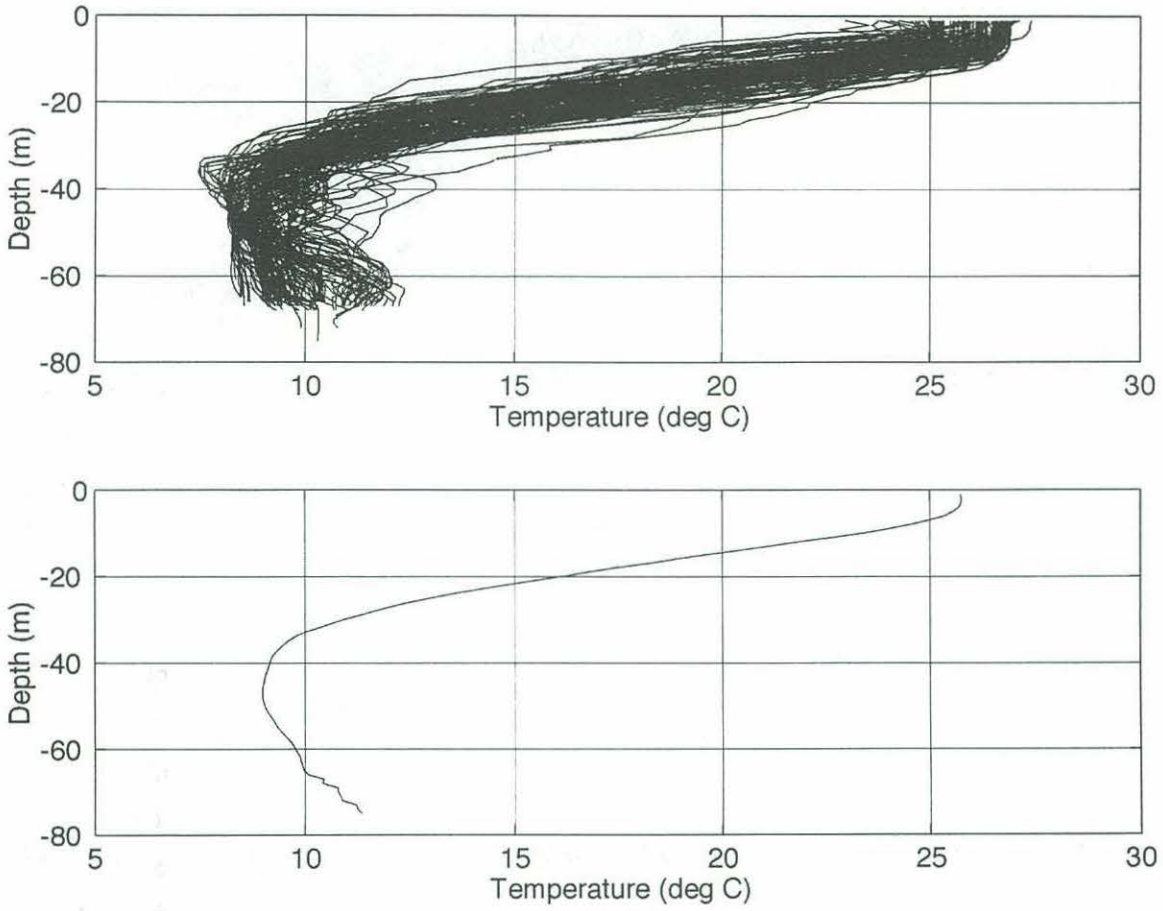

Figure 3.2: Panel one shows the temperature of 165 CTD casts done near the 75-m isobath. Panel two is the mean profile.

3.2 Salinity

Since salinity and temperature together are responsible for determining the stratification necessary for internal soliton propagation, it is important to show this field as well. The salinity of the surface mixed layer ranged from 31.4 ppt to 32.3 ppt, with a mean of 31.8 ppt (Figure 3.3). The primary halocline extended from 10 m to 20 m, followed by a reversal in the gradient, and then a more gradual decrease toward the bottom. The primary halocline increased from 31.8 ppt to 33.4 ppt, and the bottom salinity ranged from 33.3 ppt to 34.4 ppt.

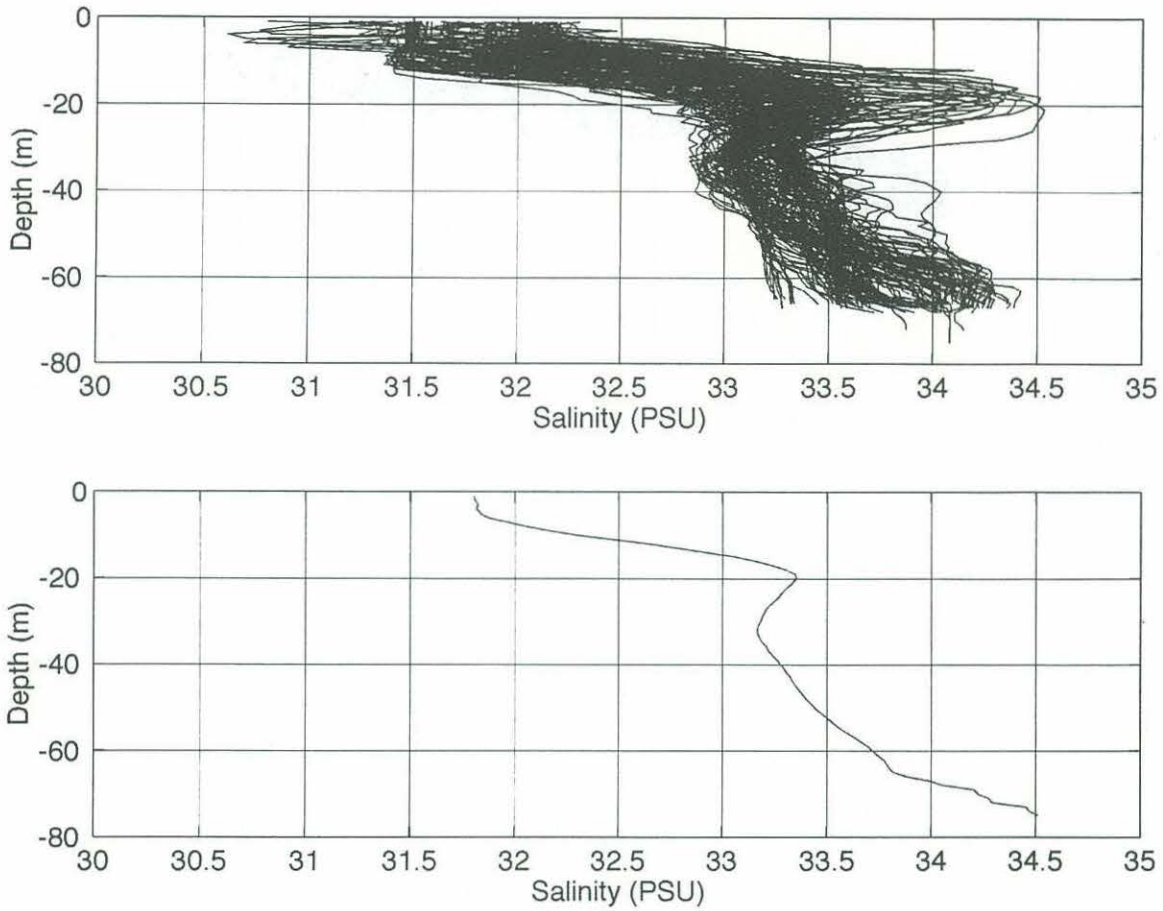

Figure 3.3: Panel one shows the salinity of 165 CTD casts done near the 75-m isobath. Panel two is the mean profile.

A useful way of seeing the temperature and salinity together is through the use of a T-S scatter plot on which lines of constant density are displayed. The isopycnals appear as curves due to the nonlinearity of the equation of state. The degree of spread in the data is apparent (Figure 3.4). The evolution of the fields in time was directly responsible for this effect. As a result, attempting to construct a functional relationship between salinity and temperature that applied for the entire experiment was inappropriate. Therefore, the salinities that were used to compute density from the thermistor data needed to be estimated in a more complex way. The method used will be discussed in Chapter 4.

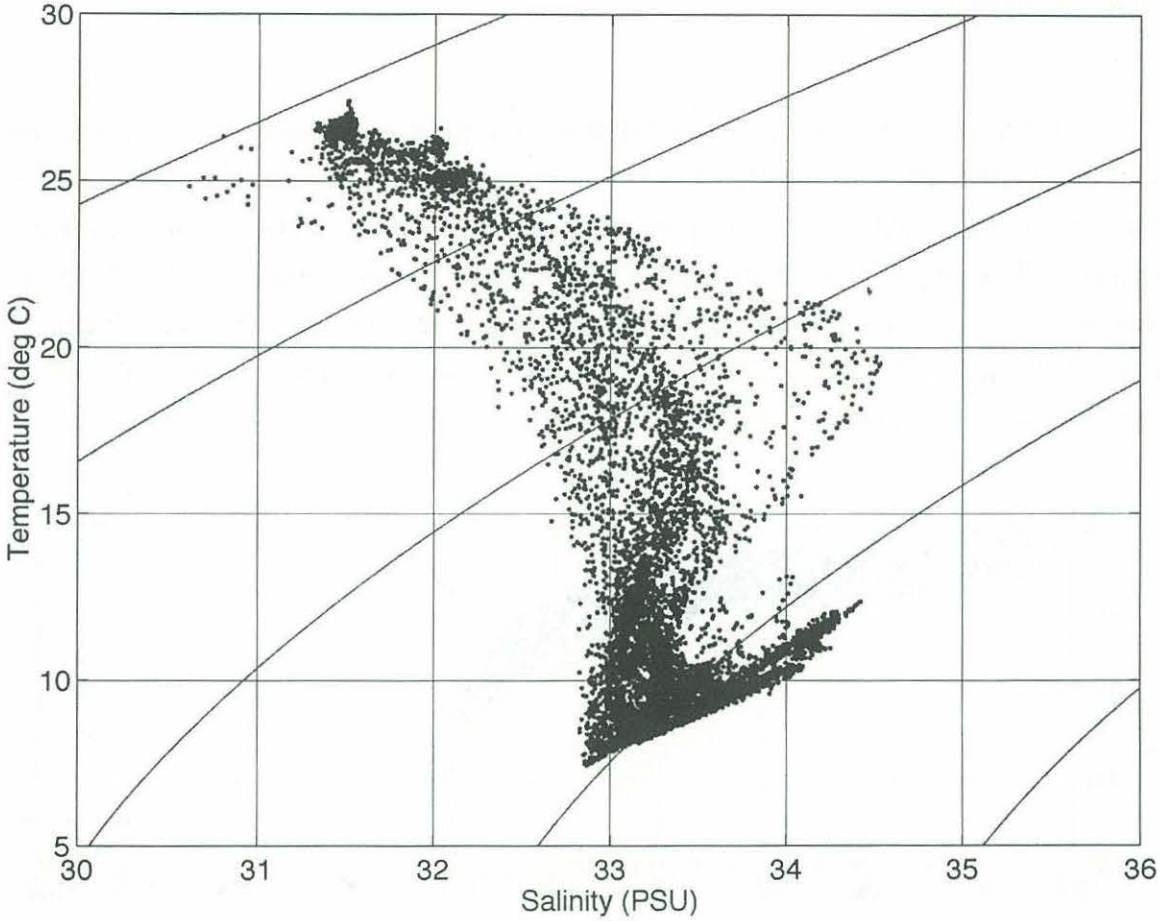

Figure 3.4: T-S plot for the CTD data collected by the *R/V Oceanus* during SWARM. Isopycnal curves are included which are in intervals of 2 kg/m^3, starting at 1020 kg/m^3 in the upper left, and stopping at 1028 kg/m^3 the lower right.

3.3 Density

Having presented the primary variables, the most important secondary quantity that merits discussion is density. Gravity and stratification provide the restoring force that the internal solitons need to propagate. The 2 - 10 m surface mixed layer had densities that ranged from 1020 kg/m^3 - 1021.5 kg/m^3, with a mean of 1020.8 kg/m^3. The mean pycnocline extended from about 5 m to 40 m, with densities that increased from 1020.8 kg/m^3 to 1025.7 kg/m^3. The bottom layer had a fairly uniform density of approximately 1025.9 kg/m^3 (Figure 3.5).

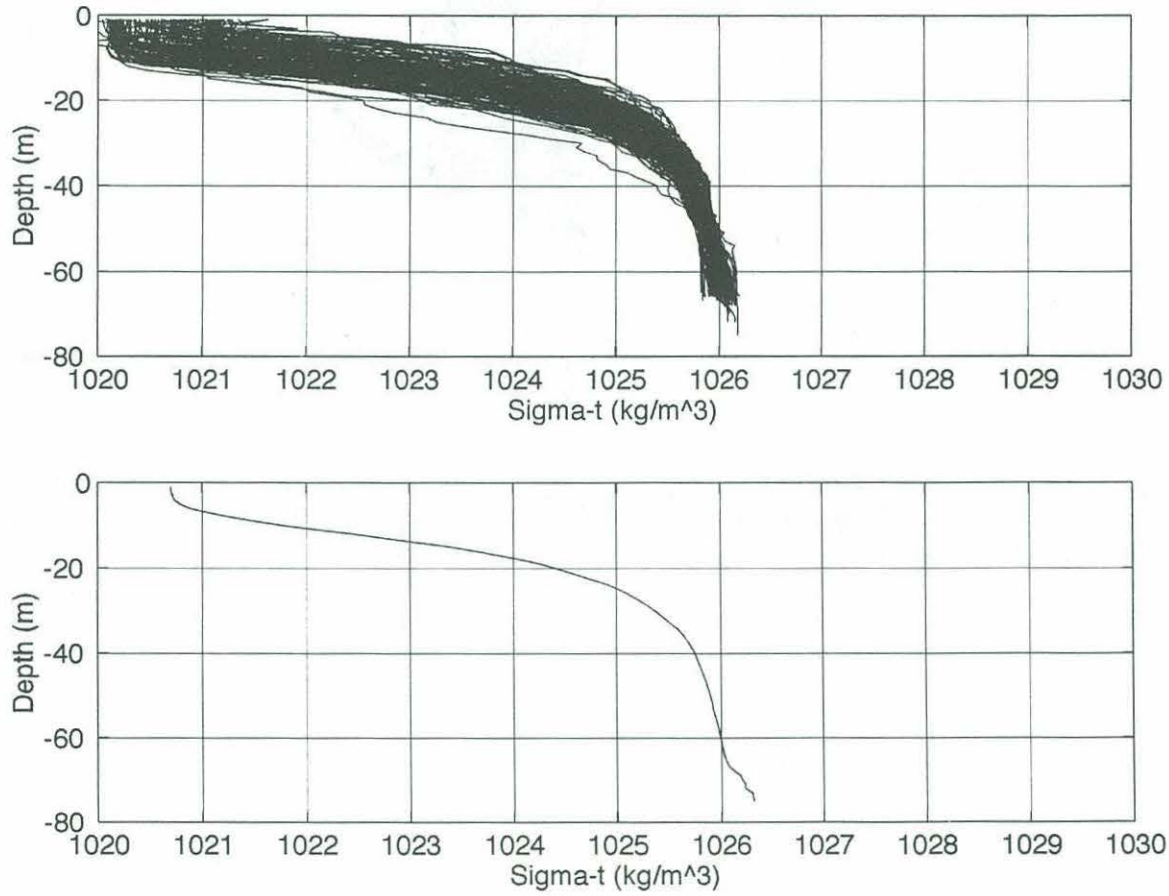

Figure 3.5: Panel one shows the density of 165 CTD casts done near the 75-m isobath. Panel two is the mean profile.

3.4 Currents

The currents associated with the barotropic tide are both the strongest signal in the SWARM region, and in combination with topography, the generation mechanism for internal solitons. As a result, I will begin by describing the currents associated with this phenomenon.

The total tidal signal is a combination of both diurnal and semidiurnal contributions. The relative importance of these constituent members depends on the specific location and shelf geometry. In order to quantify the importance of semidiurnal versus diurnal tides, *Defant* [1961] defined the following characteristic ratio,

$$F = (K_1 + O_1)/(M_2 + S_2),$$

where K_1 is the lunisolar diurnal tide (period = 23.93 hours), O_1 is the principal lunar diurnal tide (period = 25.82 hours), M_2 is the principal lunar semidiurnal tide (period = 12.42 hours), and S_2 is the principal solar semidiurnal tidal currents (period = 12.00 hours). The smaller the ratio, the more important the semidiurnal constituents are. In the SWARM region, the characteristic value based on the maximum amplitude of each tidal current is on the order of 0.25. That is, the NYB is dominated by the semidiurnal tides. In particular, the M_2 tidal current was shown to have magnitudes of up to 20 cm/s, representing the strongest of the four mentioned above.

In order for the lee wave generation mechanism to be effective, not only does the tidal current need to be energetic, but it also needs to be oriented in such a way as to produce supercritical Froude number flows. That is, if the M2 current is sufficiently energetic and has its principal axes aligned across-slope, then the production of internal solitons is more likely. In the SWARM region, isobaths are oriented at an angle of 50 ± 5° T (based on SWARM charts provided by *Jim Lynch*). This would indicate that the most favorable orientation of the tidal ellipse would be orthogonal to that direction, or 320° T. To see if this was true, I used principal axis decomposition routines on the velocity record for ADCP bins which gave the least noisy signals (the bottom seven

depth bins). What I found was that the mean orientation of the major onshore axis was ~319.3° - almost perpendicular to the isobaths (Figure 3.6).

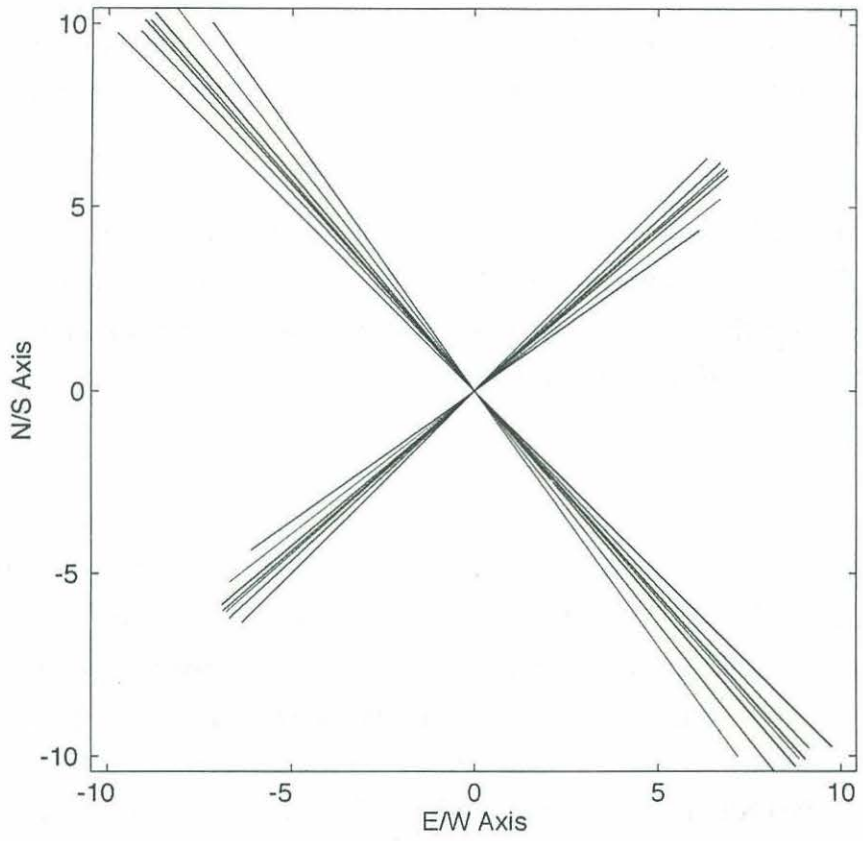

Figure 3.6: Principal tidal ellipse axes for the deepest 7 depth bins (cm/s).

Now that the orientation of the tidal ellipse was known, the normal x (East) - y (North) coordinate system could be rotated into along and across-isobath components and displayed so that the reader could better see the dominance of the barotropic M2 tide (Figure 3.7). That is,

$$u' = u \cos\theta + v \sin\theta,$$
$$v' = -u \sin\theta + v \cos\theta,$$

where u′ is the along-isobath component, and v′ is the across-isobath (onshore) component. The orientation of the isobaths, θ, is 50° T.

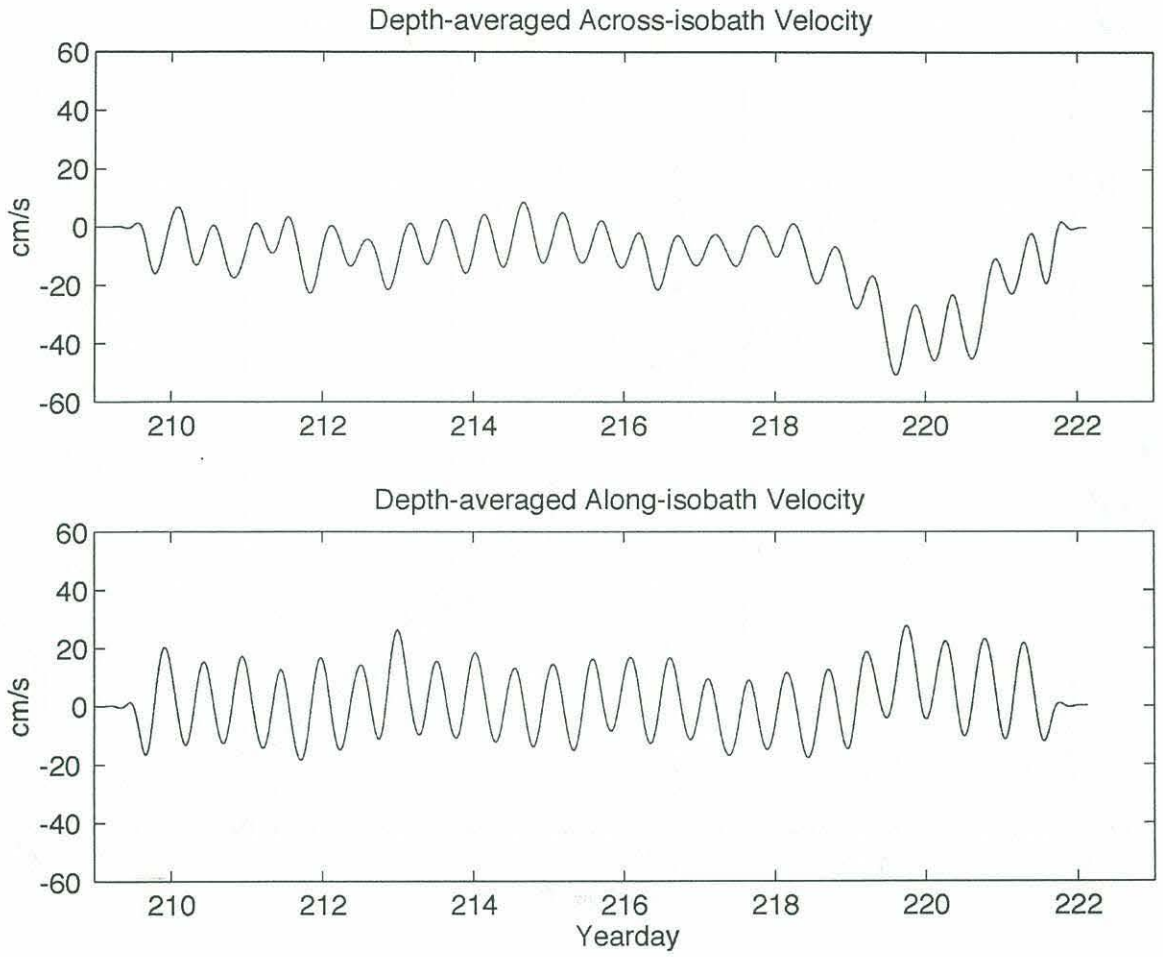

Figure 3.7: Low-pass Butterworth filtered barotropic current in bathymetric coordinates.

To aid the reader in understanding the dominance of the semidiurnal over the diurnal tides, the rotated velocities were used to compute a depth-averaged kinetic energy spectrum (Figure 3.8). With under a fortnight in duration, it is very difficult to distinguish the M2 from the S2 constituents in the spectrum. However, since the important feature that needs to be demonstrated is that the most energetic frequency band for the tides is the same as the periodicity of the soliton groups, a more careful analysis is not warranted. The spectrum shows both a semidiurnal peak with higher harmonics, and the next most dominant constituent - the O1 tide. The semidiurnal band shows up as the largest peak, surpassing the O1 by nearly an order of magnitude.

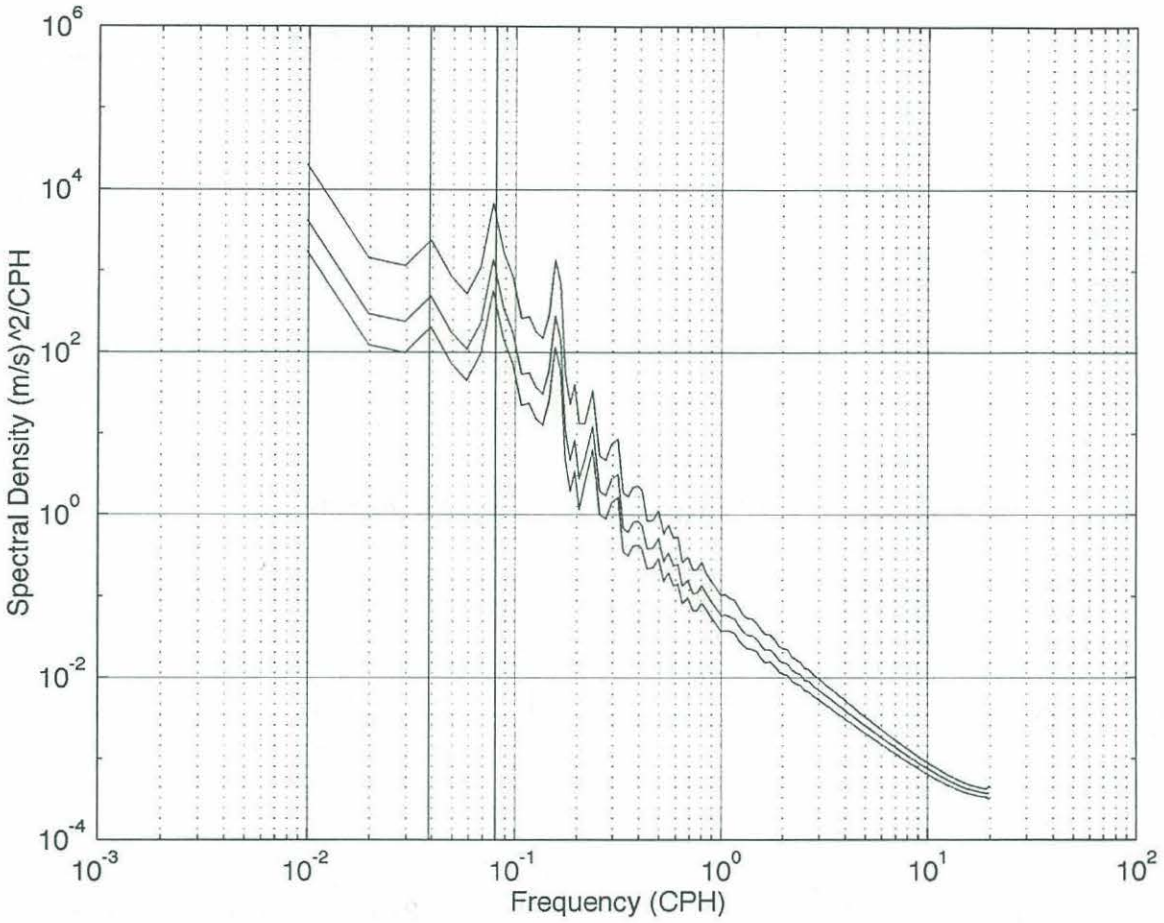

Figure 3.8: Kinetic energy spectrum for the depth-averaged velocity with the 95% confidence limits. The M2 and O1 frequencies are marked with solid vertical lines to provide a reference for the reader.

In looking at the velocity records at several depths for the duration of the experiment, one striking feature stands out - the storm of August 7 (Figure 3.9). During this storm, the winds were in excess of 35 kts. from the NNE and lasted for about a day. Whereas before the storm the currents were seen to rotate through 360°, during the storm the winds induced a large enough signal to effectively prevent the tidal ellipse from tracing out its typical rotary path. Since the winds were blowing out of the NNE, approximately parallel to the local isobaths and regional topography, the primary

current response was a strong (about 40 cm/s), roughly barotropic current pulse in the down and slightly on-shelf direction (WSW).

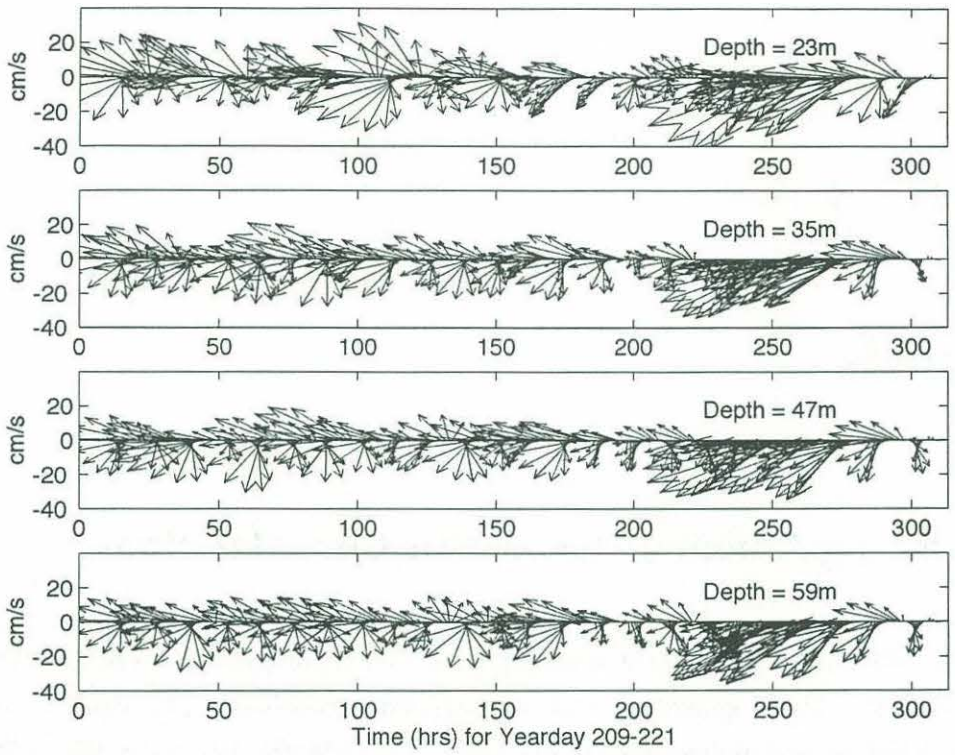

Figure 3.9: Feather plots of ADCP velocity. Note the storm event of hours 200 - 250.

What this suggests is that the generation mechanism was reduced or inhibited during the storm due to the reduction of off-slope current. Appendix B provides some other figures which may help elucidate this phenomenon further.

Chapter 4

Analysis

4.1 T-String Antenna - Geometric Considerations

The best way to explain the meaning of a T-string antenna is to draw the layout and show how simple geometric and trigonometric considerations can be used to determine heading and phase speed information. Consider the following diagram:

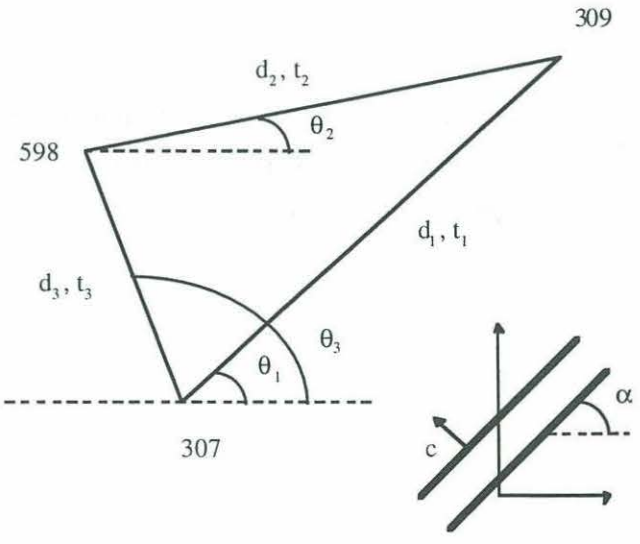

Figure 4.1: Position diagram detailing the relative location of the thermistor strings.

In this diagram, what is pictured is the location of T-strings 598, 309, and 307 - the vertices of the triangle. The distance separating each of these and the time it would take an internal soliton (with phase speed c and orientation α) to travel between them are given by d and t respectively (where the subscript denotes a particular path). From this configuration, one can write down the following expressions for the transit time along the three paths:

$$t_1 = [d_1 \sin(\alpha - \theta_1)]/c,$$
$$t_2 = [d_2 \sin(\alpha - \theta_2)]/c,$$
$$t_3 = [-d_3 \sin(\alpha - \theta_3)]/c,$$

from which we can easily write the matrix equations

$$\begin{vmatrix} \cos\theta_1 & -\sin\theta_1 \\ \cos\theta_2 & -\sin\theta_2 \\ \cos\theta_3 & -\sin\theta_3 \end{vmatrix} \begin{vmatrix} \sin\alpha / c \\ \cos\alpha / c \end{vmatrix} = \begin{vmatrix} t_1/d_1 \\ t_2/d_2 \\ -t_3/d_3 \end{vmatrix}$$

where

$$d_1 = 1058.7 \text{ m} \qquad \theta_1 = 45.5°,$$
$$d_2 = 794.8 \text{ m} \qquad \theta_2 = 8.8°,$$
$$d_3 = 634.3 \text{ m} \qquad \theta_3 = 93.9°.$$

Solving the matrix equations and using the definitions

$$\varphi_1 = \sin\alpha / c,$$
$$\varphi_2 = \cos\alpha / c,$$

we get

$$\alpha = \arctan(\varphi_1/\varphi_2),$$
$$c = [(\varphi_1)^2 + (\varphi_2)^2]^{-1/2}.$$

These expressions for α and c can be used for each internal soliton whose transit time for the three paths can be accurately determined.

4.2 T-String Antenna - Technique

In order to best pick out the internal solitons during a given time frame, the original temperature signals for each thermistor on each string were high-pass filtered using a Butterworth filter with a cutoff period of 36 minutes. This effectively removes the tides and other lower frequency phenomena. Since the primary goal was to determine the delay times along each of the three tracks, it was necessary to pick out the time when each internal soliton encountered the three moorings. Then, by simple subtraction the observed delays can be quantified.

To do this, the high-pass time series were contoured as a function of depth and time for each six hour period from the beginning to the end of the experiment. Each of the contoured fields for the three T-strings were then displayed simultaneously so that similar solitons could be isolated in all of the records. Typically, on the order of five internal solitons per packet were seen at each mooring. To pin down a characteristic time for each soliton, a point and click technique was employed using the mouse and crosshairs provided by the "ginput" function in Matlab. The crosshairs were placed as close to the soliton peak as possible at a depth were it was very clear. Then, an automated routine looked for the time at which the maximum temperature deviation occurred in the vicinity of the stored time for each of the instruments. The arrival time was then the average of the times found for each of the eleven instruments on the T-string. This was repeated for every soliton in every six hour period for the entire record.

With the observed delay times in hand, it was a simple matter to calculate the bearing and phase speed for the internal solitons in each packet. However, while the bearing this time delay gives is the same as the bearing that was observed on the ship's radar and by other remote sensing systems (and therefore the pertinent one) flow [*J. Lynch,* personal communication], the phase speed is actually the phase speed as embedded in the background flow. In other words, depending on the strength and orientation of the background flow, the phase speeds that this technique gives you can be very badly skewed. As a result, in order to determine actual phase speeds, a procedure for calculating and removing the ambient flow field from the estimations was required.

This was accomplished through the use of the ADCP data. I assumed that the measured velocity field at the ADCP site during the period that each internal soliton packet was passing through the antenna was identical to the flow field at the antenna. This approach seemed reasonable since the center of the antenna was located only 1.2 km to the NW of the ADCP, and the shelf-slope front was generally located well offshore of the combined array. In effect, the ADCP was used to provide the background flow field which could be factored into the calculation of phase speed. That is, knowing the phase speed as calculated from the antenna and the time evolution of the velocity field at the ADCP, the true phase speed for the solitons could be extracted.

4.3 Displacement Calculations

Although this thesis will not address the energy content of the internal soliton field directly, it will attempt to describe the nearest proxy to that quantity - the vertical displacements. Since there was no instrumentation deployed which directly measured the vertical displacements associated with the internal solitons, this quantity needed to be inferred from the available data. Several options were considered. The first option was to use the vertical velocity field as measured by the ADCP. This method required accurate estimates of the vertical velocity which can then be integrated over the water depth to produce estimates of displacement. This seemed like an appealing method since it required no creative manipulation of the data, however it fell short due to the

inherent noisiness in the measurement of vertical velocity. As a result, another option was used.

The thinking behind method two is as follows. Physical intuition dictates that as these solitons pass a given location, they perturb a field which provides a surface on which the disturbance can propagate. The surface in this case is the pycnocline layer which then seeks to return to a stable depth after the passage of the disturbance. The restoring force responsible for this rebounding of the pycnocline is gravity. As a result, one might expect that a reasonable relationship between density perturbations and vertical displacements can easily be found. In fact, this is the case and the relationship takes on the form [*Wallinga*, 1996]

$$\zeta(t) = \sigma_\theta'(t) \; / \; [\partial \sigma_\theta / \partial z],$$

where $\sigma_\theta'(t)$ is the perturbation density field which is the high-pass time series of density and is comprised of the solitons alone. The denominator of the above expression, $[\partial \sigma_\theta / \partial z]$, is the mean background gradient against which work must be done to displace the pycnocline by a given amount. The problem here was that no direct time series measurements of salinity existed in-situ with the thermistors, so density was not a quantity whose calculation was immediately obvious.

As described in Section 1.2, the *R/V Oceanus* had as one of its primary responsibilities the collection of hydrographic data near the moored array site via yo-yo CTD operations. As a result, salinity measurements exist throughout much of the experiment, with several interludes during which no casts were done. Using these data in tandem with the T-chain thermistor data, I was able to construct a suitable density record from which vertical displacements could be calculated. The procedure was automated to pick out those CTD records that fell within an hour on either side of a particular data point in the T-chain temperature series. If no data were found, the range was increased iteratively until data existed. Once the CTD record nearest in time was identified, the procedure extracted the CTD salinity associated with the CTD temperature that matched the T-chain temperature. Thus, for every T-chain temperature point, a corresponding CTD salinity value was obtained. The resulting T-chain temperature and CTD salinity time series were then used to compute a density time series for each instrument. Periods where the gap between CTD casts and T-chain

samples were larger than 6 hours were excluded from further analysis for vertical displacements. Although this approach is certainly not ideal, it is the only way that I found to be both tractable and believable. I should note that since this process involved the creative use of the CTD records (which numbered more than 160 casts), I also checked the difference between the expression for displacement above with one which used T-chain temperature data solely. The results, while differing in exact magnitude, maintained the soliton structure and character. As a result, it seemed safe to assume that the vertical displacement field obtained for the combined T-chain and CTD yo-yo data is valid.

4.4 Analysis of Clearest Rank-ordered Group

In order to present information about the statistics of a typical rank-ordered group, I have singled out one of the clearest packets for the sake of clarity. This particular group was recorded moving through the area between yeardays 210.9 and 211.1 and was comprised of five solitons. The solitons within this group arrive at the three T-strings with timings that are consistent with an onshore movement of the phase, and appear to have the proper rank-ordered format (Figure 4.2).

In the early sections of this thesis, I pointed out that an internal soliton's capacity to impact the environment through which it passes is one of the primary reasons they have generated such a large amount of interest in recent years. Their role in mixing, frontal maintenance, tidal dissipation, and vertical flux of nutrients and organisms are just a few of the possible influences solitons can have. This list should also include the complications they introduce for the use of acoustics as an oceanographic tool - the primary purpose of SWARM. The larger the energy content of a given soliton, the more likely it will play a role in some of these areas. Since the displacement is a direct reflection of this energy, it is a reasonable field to investigate and characterize. On top of this impetus, we also seek to verify the dynamic architecture of the finite-depth theory which has so far seemed appropriate.

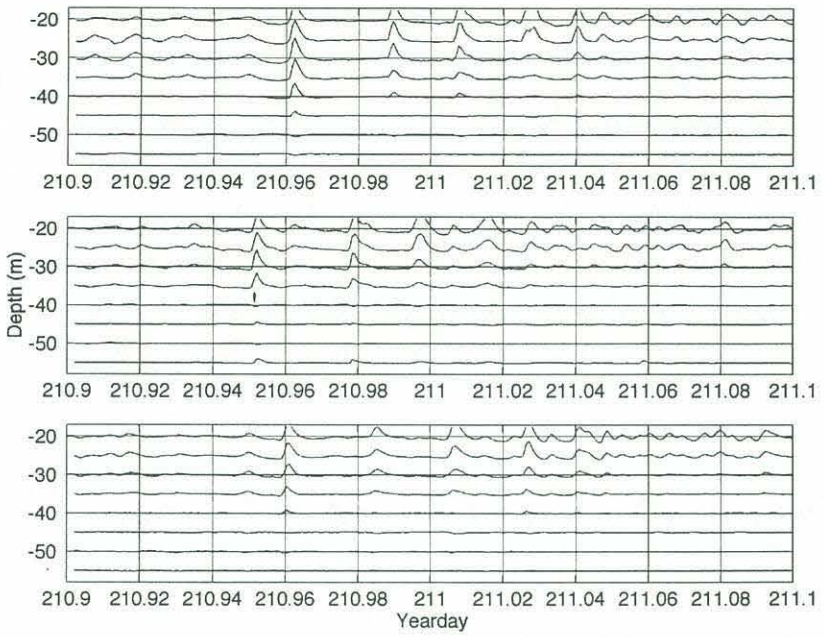

Figure 4.2: Temperature contours of a rank-ordered group of solitons - 1 m variation corresponds to 1° C. Note the timing as well as the amplitudes of the solitons at each thermistor are in agreement with rank-ordered onshore propagation. The top, middle, and bottom panels correspond to T-string 598, 309, and 307 respectively.

The displacement calculations involved determining a density field by combining both the T-string time series and CTD profile data. Without looking at the vertical velocity field, this is perhaps the best way of arriving at a believable estimate. Recall that the estimate of displacement was determined by the perturbation density field divided by the background vertical gradient,

$$\zeta(t) = \sigma_\theta'(t) \; / \; [\partial \sigma_\theta / \partial z].$$

The most questionable aspect of this calculation is the use of a given salinity field during times which CTD casts were not being done. However, since SWARM was conducted in a region where frontal advection effects were small, this approach is acceptable.

The issues which we wish to investigate are the following: the shape of the solitons - do they resemble the familiar $\mathrm{sech}^2(x)$, are the depressions downward from the pycnocline - since $h_1/h_2 < 1$, and do the maximum displacements occur at the pycnocline

where the onshore particle velocities change sign - since that is the location of the maximum vertical velocities.

To address the first question, I examined displacements during energetic periods (Figure 4.3). This showed that the signal was not a sinusoidal wave but rather a series of singular pulses. These pulses do not possess the smoothness of a theoretical $\text{sech}^2(x)$ profile, but they are qualitatively a close approximation to it. This can be seen better in Figure 4.4, where the lead soliton is shown with an expanded time axis. This figure also illustrates a "memory" effect. That is, when a soliton passes a location, the depth where one finds a given isopycnal is deeper after the passage than before. The water column has been perturbed in some way that extracts energy from the soliton and leaves the stratification changed. Ongoing research of *Apel* and others has had recent success at modeling this effect [*J. Apel*, Personal communication].

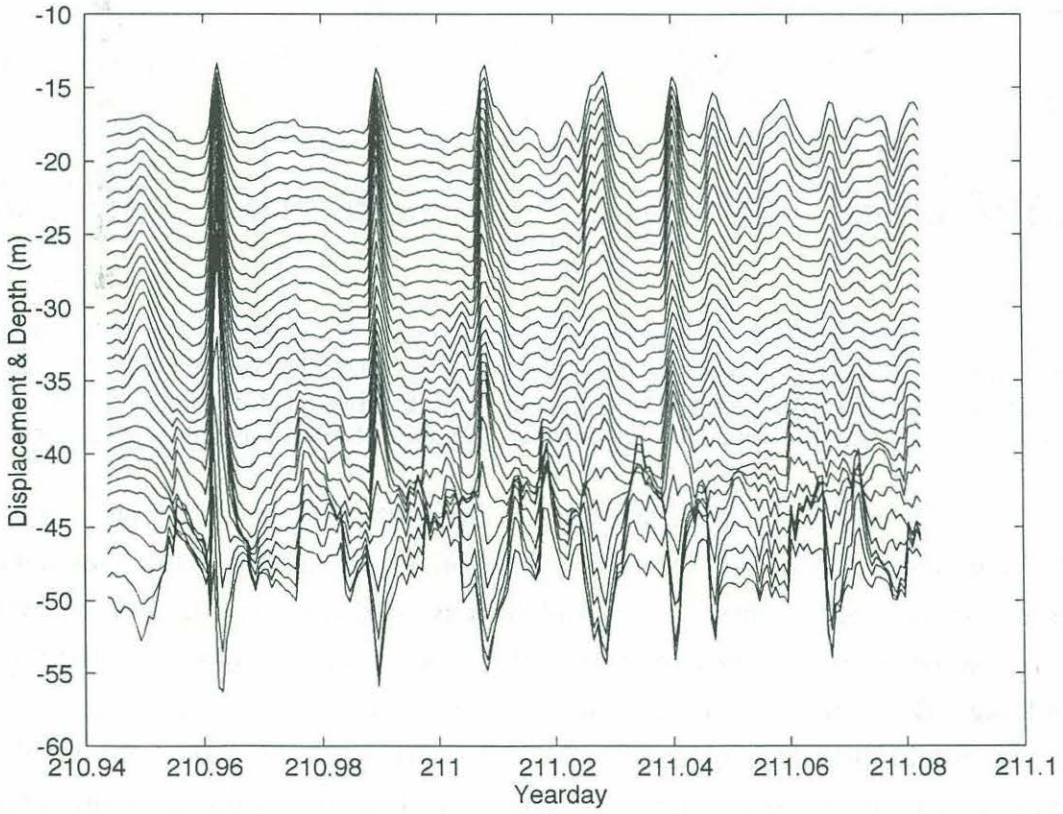

Figure 4.3: Displacement time series plotted at measurement depth. The temperature data was gathered using T-string 598. Note the presence of five large amplitude internal solitons. *Nota Bene: Positive displacements are measured downward.*

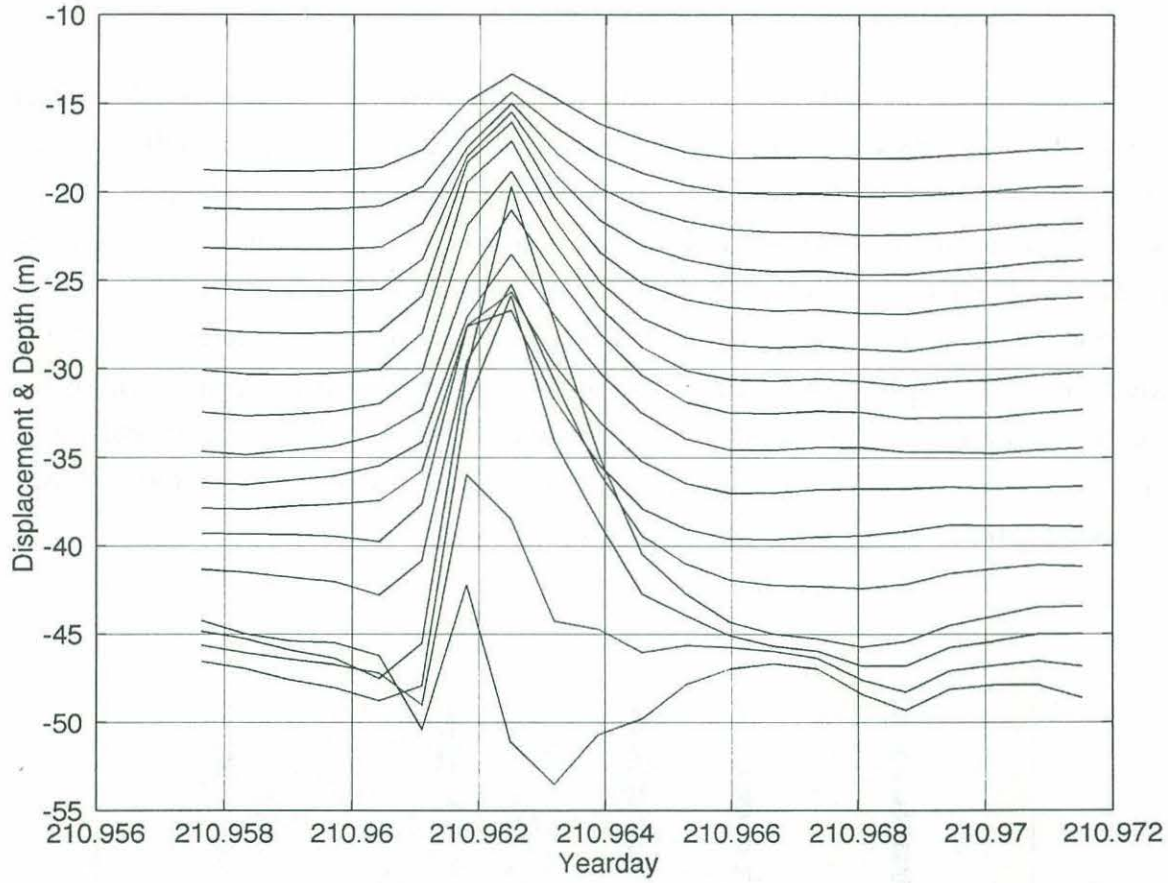

Figure 4.4: Blowup of the lead soliton in the yearday 210.9 - 211.1 group. Note that the shape approximates the classic KdV $\text{sech}^2(x)$ profile. The "memory" that the system has that an internal soliton passed by is represented by the net downward displacement of the isopycnals. As in Figure 4.3, positive displacement are measured downward.

To determine the vertical structure of the soliton field, I next performed EOF analysis on the ADCP velocity record as a function of depth. Before this was done, an accurate estimate of the mean background velocity field was computed and removed. This was accomplished in the same way that the phase speeds were corrected for flow imbedding. The result was that the most energetic velocity mode was indeed the first baroclinic mode which was responsible for 87.5% of the variance of the total signal. The next most energetic mode contained a meager 7.6%. To illustrate this structure a plot of the velocity for each of the five solitons in the yearday 210.9 - 211.1 event is included (Figure 4.5). The time of each profile corresponds to the time when the maximum

displacement was centered over the ADCP. Note that while variation exists among these solitons, the character of each is undeniably consistent with mode one structure. The fact that the velocity in the lower layer carried a significant depth dependence also suggests that finite-depth theory is more appropriate than shallow-water theory.

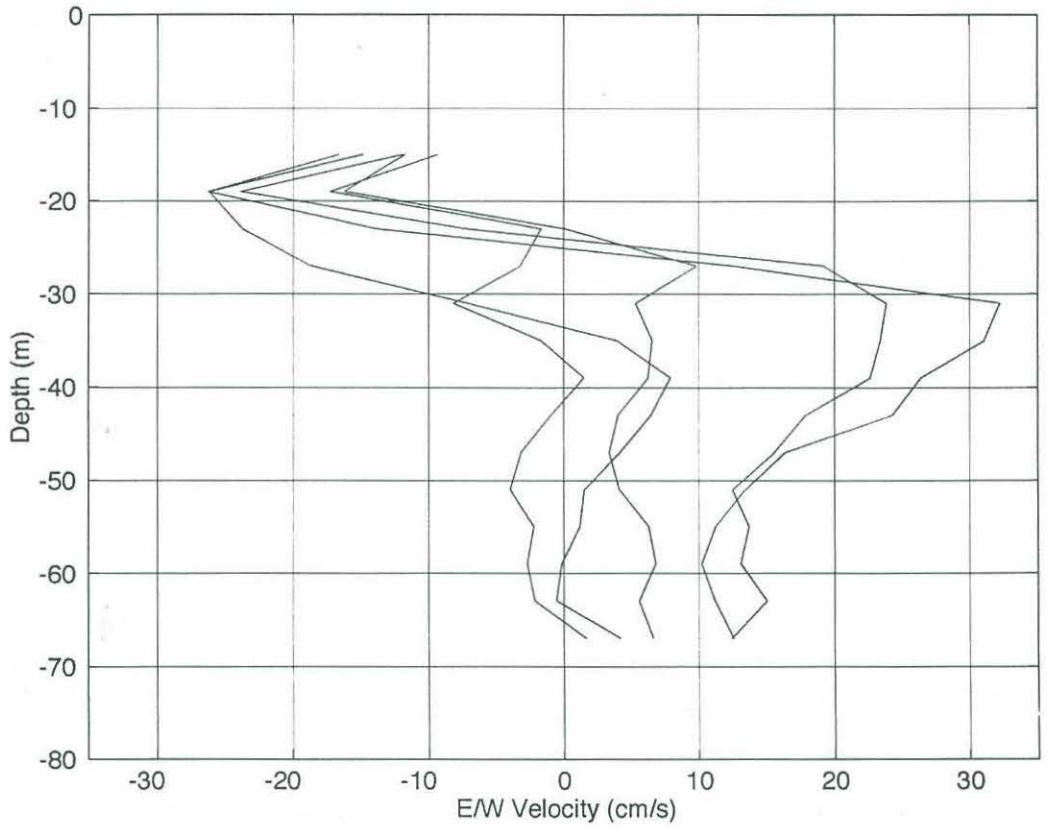

Figure 4.5: Vertical profiles of E/W velocity for solitons of yeardays 210.9 - 211.1.

To test finite-depth theory, the phase speed should be considered. Recall the predictions that were outlined in Section 2.3. The phase speed of the solitons in a rank-ordered group should exceed the linear phase speed by a predictable amount. That amount depends on the stratification, the effective upper layer depth h_1, the total depth H, and the amplitude η_o. The stratification parameter requires the choice of an upper and lower layer density (ρ_1 and ρ_2 respectively). Since to first order the stratification is two-layered, a least-squares analysis was used to find the densities and the effective upper layer depth. The profile that was used was the mean of the density profiles just

before and just after the rank-ordered group passed the array. The result of that fit was $h_1 = 21.9 \pm 3.4$ m, $\rho_1 = 1021.21 \pm 0.08$ kg/m^3, and $\rho_2 = 1025.98 \pm 0.06$ kg/m^3 (Figure 4.6).

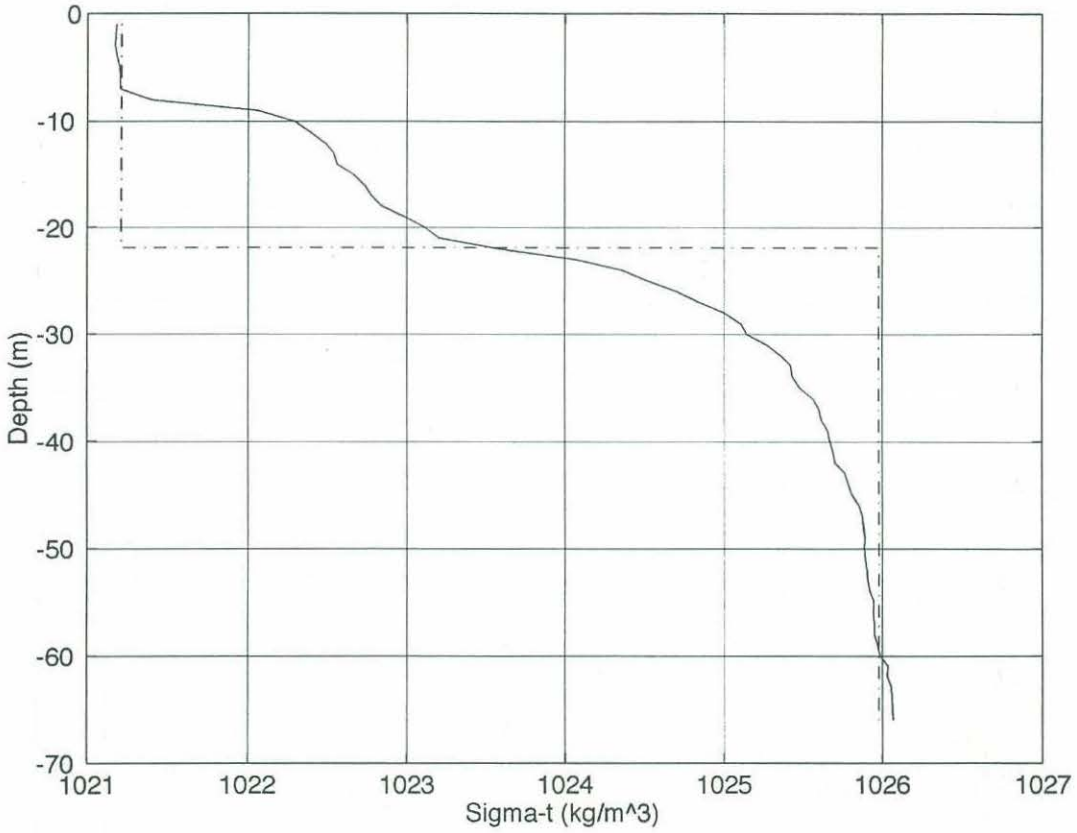

Figure 4.6: Mean density profile during 210.9 - 211.1 event, including least-squares fit to a two-layer model.

The displacement amplitude η_o used in the estimation of phase speed for this model was the maximum displacement in the vicinity of the depth h_1. These values were then used in the formulas of Section 2.3 to see how accurate the finite-depth model was in predicting phase speeds and horizontal scales. Figure 4.7, Figure 4.8 and Table 4.1 summarize the results.

	Soliton 1	Soliton 2	Soliton 3	Soliton 4	Soliton 5
η_o (m)	9.8	5.6	4.7	2.0	3.2
b (m)	65.3	114.2	136.1	319.7	199.8
a (m^{-1})	0.012	0.0098	0.0093	0.0061	0.0078
c_o^{pred} (m/s)	0.84	0.84	0.84	0.84	0.84
c^{pred} (m/s)	1.02	0.94	0.92	0.88	0.89
$c^{measured}$ (m/s)	0.83	0.77	0.66	0.57	0.55
$L^{predicted}$ (m)	48.4	70.2	77.2	127.7	95.5
$L^{measured}$ (m)	48.0	66.5	71.7	99.7	83.3

Table 4.1: Phase speed and horizontal scale comparison of finite-depth model and data for the yearday 210.9 - 211.1 group. The mean group heading was 269.9 ± 11.0° T. The above values for a, b, and L were calculated by $b = 4h_1^2/3\eta_o$, $\tan(aH) = 1/(ab)$, and $L = \{\cosh^{-1}[(1 + 3(ab)^2)/(1 + (ab)^2)]\}/(2a)$.

As noted in Chapter 2, the finite thickness of the pycnocline effectively reduces the phase speed from the linear two-layer prediction, so it is not surprising that the observed phase speed is smaller than given by the two-layer finite-depth theory. For the largest two solitons, the slope of the observed phase speed change with η_o is qualitatively similar to that predicted by finite-depth theory (Figure 4.7). In terms of the horizontal scale L, finite-depth theory does a fair job at predicting the scales of the of the most robust members of the group (solitons 1 - 3), but falls short when looking at the last two (Figure 4.8). Soliton 4 is the most poorly understood member, with unusually small displacements that in turn cause large predictions for the horizontal scale.

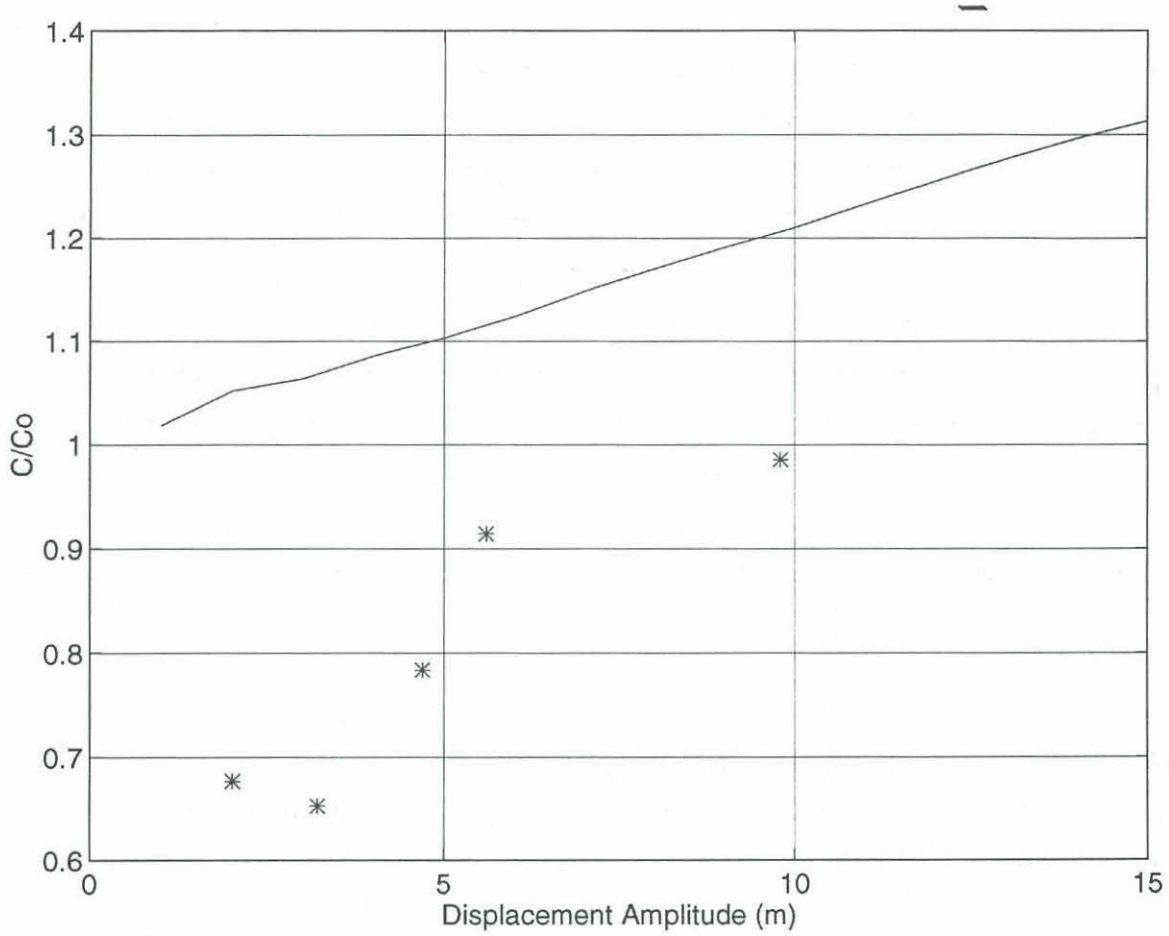

Figure 4.7: Comparison of finite-depth theory predictions for phase speed (solid line) with the data (asterisks). Note that for the largest solitons in the group, the slope of a line drawn through the points is nearly identical to the theoretical slope. The theory is shown to consistently overpredict the observed values.

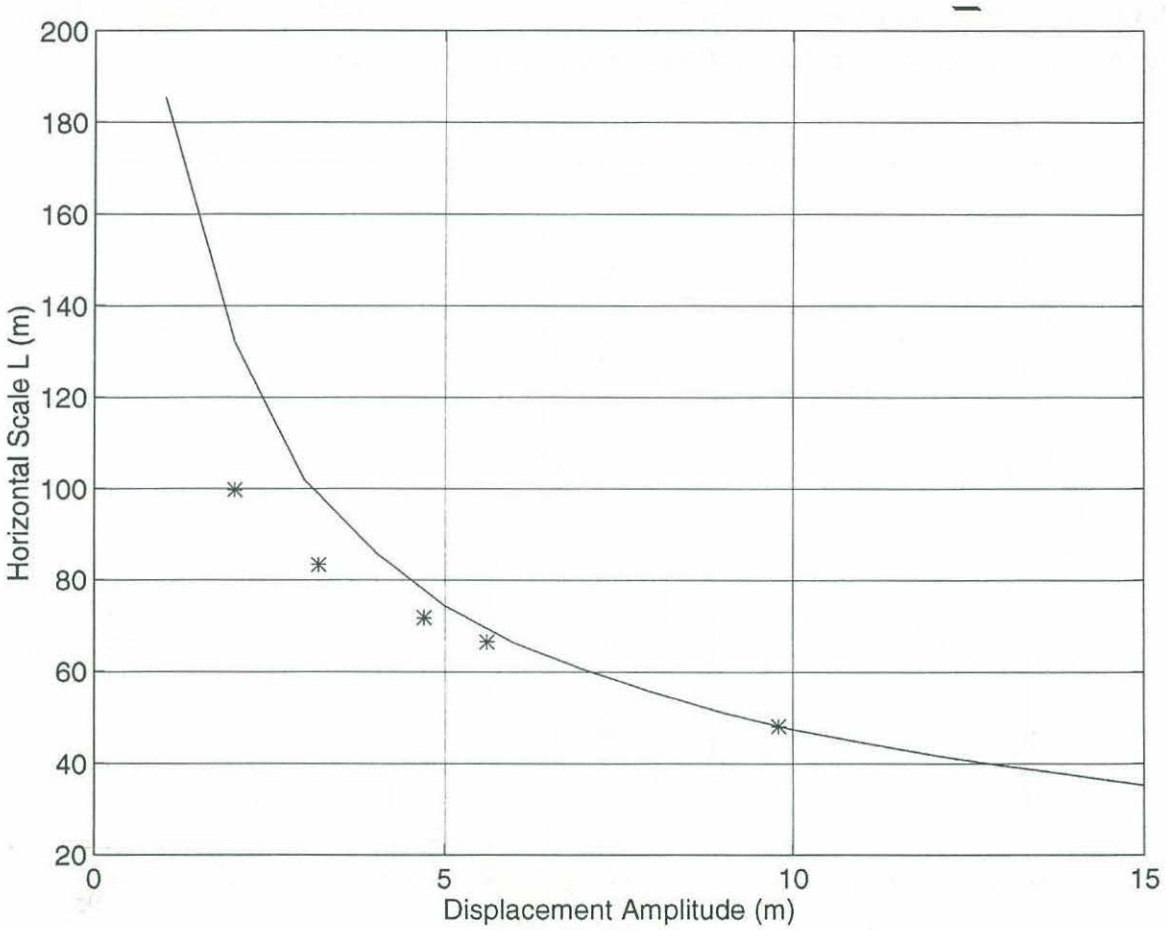

Figure 4.8: Comparison of finite-depth theory predictions for the horizontal scale L (solid line) with the data (asterisks). Note that for the largest solitons in the group, the agreement seems better than for the smaller members.

4.5 Analysis of Entire Soliton Record

The phase speed of each member soliton in a given rank-ordered group is not the same. The fact that the phase speed is a function of the amplitude of the soliton is precisely why the rank-ordered group develops in the first place. As a result, the largest solitons move out ahead of the smaller ones and the phase speed characteristics therefore have some spread in magnitude. On top of this, the phase speed also depends on the ambient stratification. Therefore, if the stratification changes, so will the observed speeds. In total, there are many other smaller effects, not the least of which is the spring-neap cycle, which can affect the distribution of soliton phase speeds. Due to

these functional dependencies, the results do not show distinct groupings of phase speeds that correspond to the position in each group (Figure 4.9).

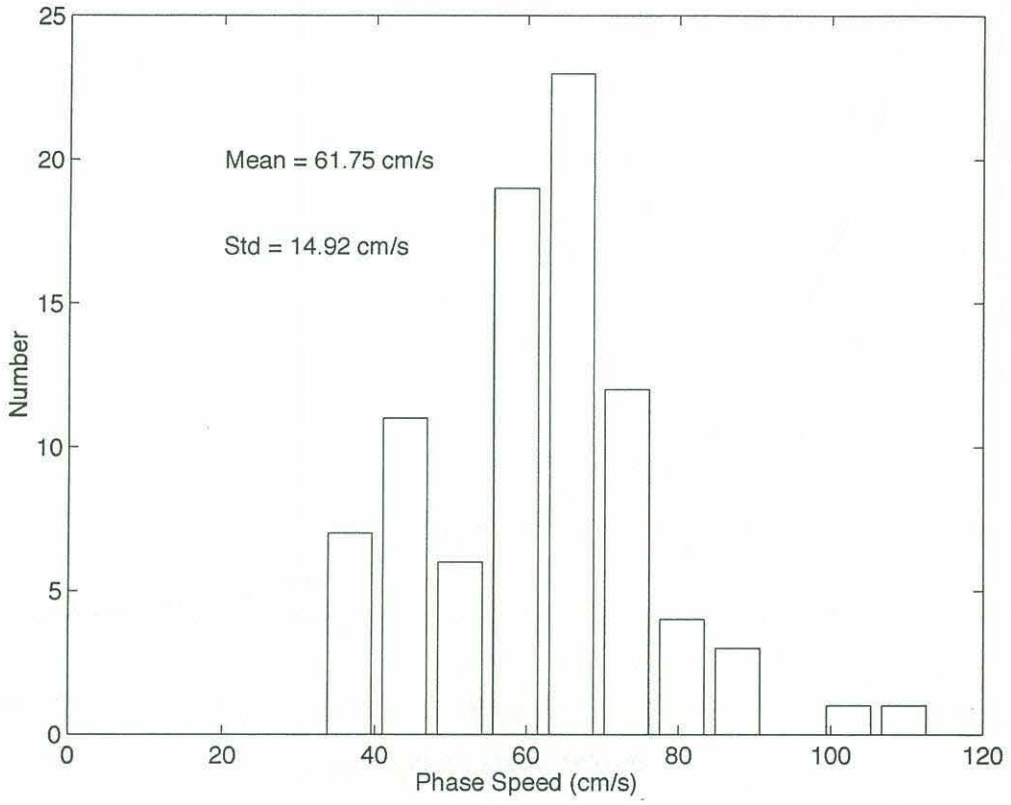

Figure 4.9: Histogram of soliton phase speeds. The total number characterized was 87.

The heading of these solitons was determined from the full velocity field and the arrival times at each of the three T-strings in the antenna. Since the fluid velocity associated with a given soliton is in the direction of propagation in the upper layer and opposite to it in the lower layer, we expect to see headings that change in the vicinity of the pycnocline. That is, the heading determination was carried out for all available depths and the distribution of those headings was shown to be consistent with that fact. The results of the analysis are clearest in the middle of each layer and become unclear in the vicinity of the layer depth change. Taking that fact into account, we get a mean heading for a typical packet of about 280 ± 31° T. Table 4.2 shows the result of the analysis for each depth, while Appendix C provides the histograms that go along with it.

Depth (m)	Heading (deg. from N)	Standard Deviation
67	170.3	68.8
63	162.6	67.2
59	163.2	65.4
55	163.7	66.8
51	173.8	61.8
47	181.3	62.0
43	189.1	63.3
39	180.1	65.2
35	179.8	72.1
31	184.8	81.0
27	188.1	94.9
23	237.3	91.5
19	279.5	31.0
15	270.1	44.2

Table 4.2: Soliton heading as a function of depth during SWARM.

It should also be noted here that these numbers represent the heading of the clearest rank-ordered groups and are not meant to indicate that all solitons had this bearing. Rather, it simply implies that the ones which could be best characterized were those that were generated in a region that yielded this heading.

The last feature of the displacement time series I wish to discuss is the characteristic depth of the maximum displacements. To compliment this information, typical magnitudes are also described. As mentioned above, the maximum displacement should be coincident with the depth of maximum vertical velocity. The vertical velocity is maximum at the interface and decays both above and below that depth. Since the effective layer depth has been seen to be somewhere between 20 m and 30 m during SWARM, what we expect is to find solitons whose displacement structure mirrors this fact. To best show this information, I went through the displacement record

in exactly the same way as the T-string data. I made daily subplots of the time series and chose the peak of each clear soliton that was observed. Some were much clearer than others, but due to the fact that stratification may have been inhibiting or encouraging large amplitudes, I extracted all potential events. I then made vertical profiles of all the events and plotted them on the same plot for the region of maximum displacements. As it turned out, all of the maxima fell between 20 m and 35 m depth (Figure 4.10). Some spread did exist, but the overwhelming evidence is in support of the claim made above.

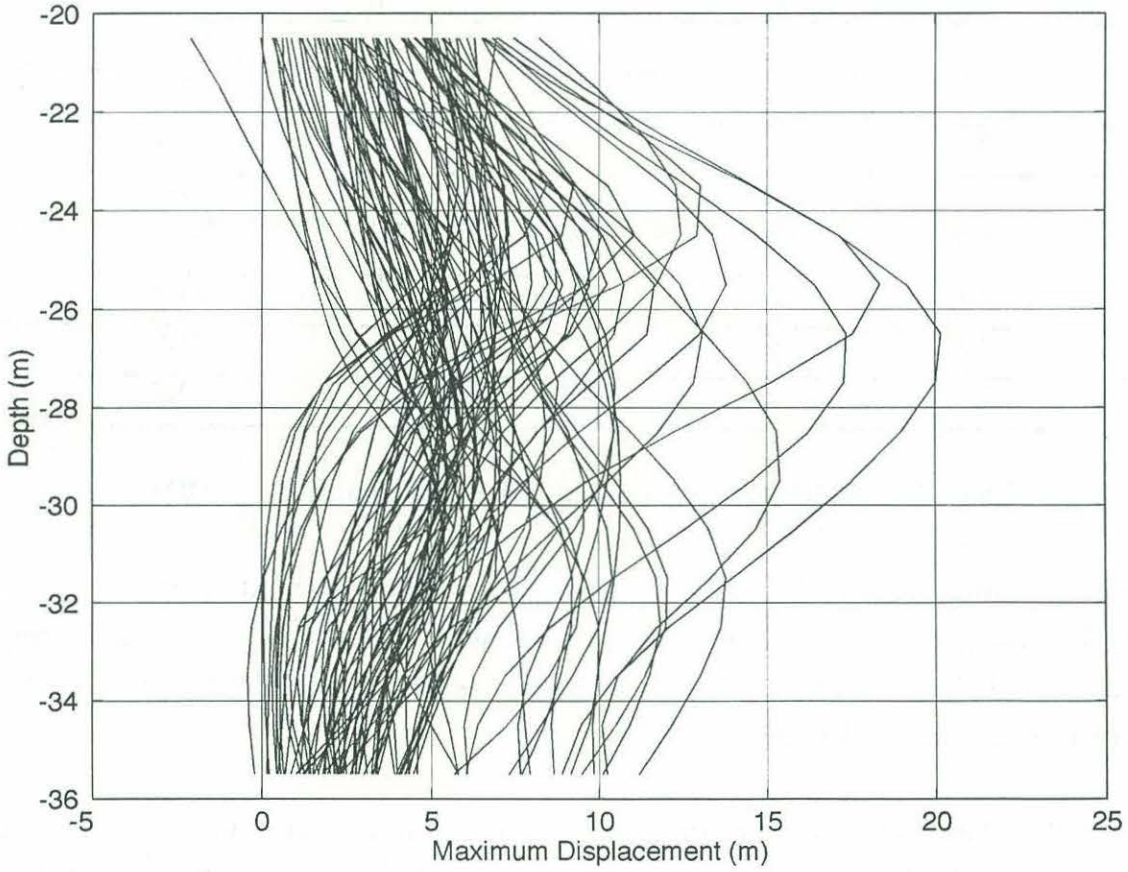

Figure 4.10: Vertical profiles of maximum displacements in the pycnocline region.

The range of maximum amplitudes for the internal solitons is quite large, but has a fairly convincing mean structure (Figure 4.11). Although some of the largest solitons had magnitudes up to 20 m - quite significant in just 75 m of water, the mean was actually

quite a bit lower at 4.75 m with a standard deviation of 3.26 m. As it turned out, the large solitons appeared in the first several days, with the very largest clustered around yearday 212. Toward the end of the record, the magnitudes never exceed 10 m, and less than 5 m for yeardays 216 - 217 (Figure 4.12).

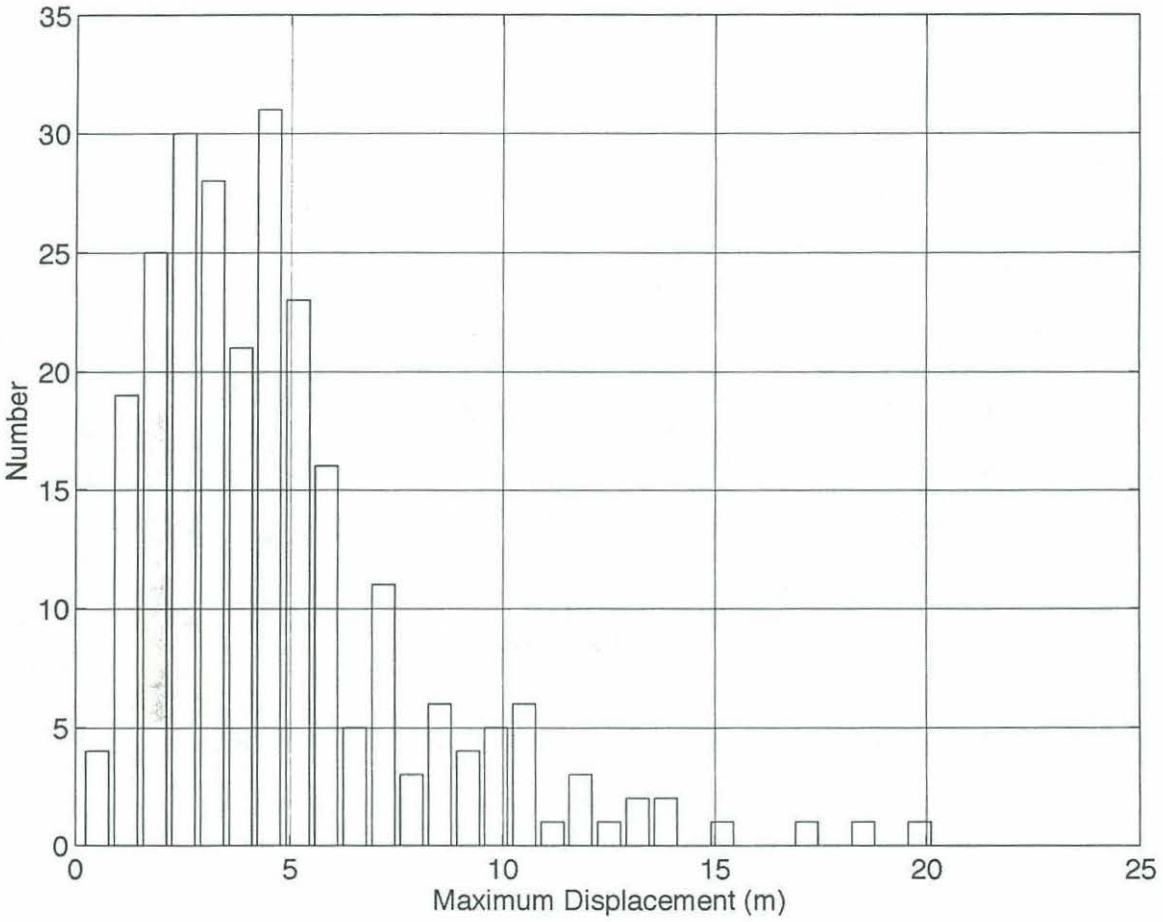

Figure 4.11: Histogram of maximum displacements spanning yeardays 210 - 218.

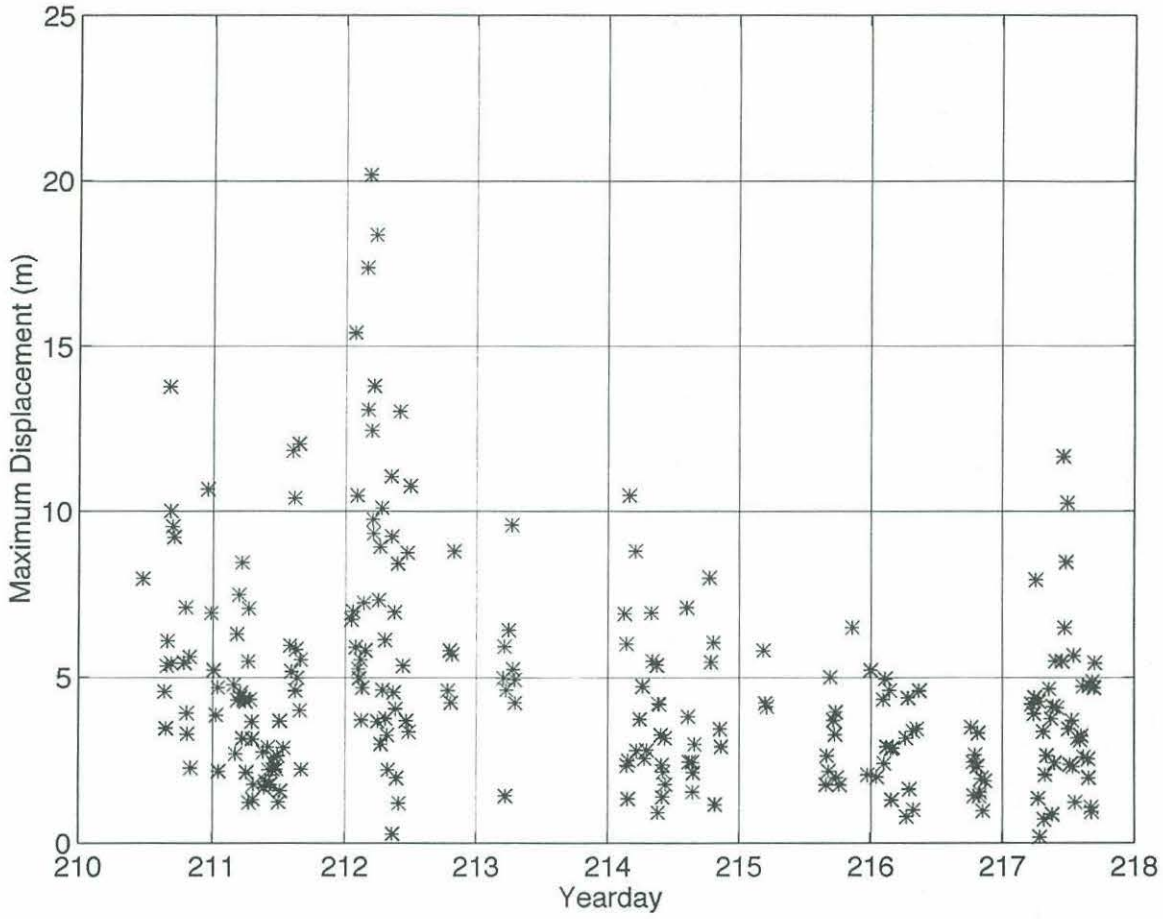

Figure 4.12: Scatter plot of temporal structure for soliton maximum displacement field.

Chapter 5

Summary and Conclusions

The SWARM experiment conducted in the NYB in late summer 1995 provided an enormous amount of data, both physical and acoustic, which showed a rich environment full of large-amplitude internal disturbances. These disturbances are presumably generated at the shelf break by the interaction of the barotropic semidiurnal tidal current and bottom topography. During the nearly two-week period of data collection during SWARM, thermistor strings and an ADCP obtained high-frequency time series of temperature and current. Numerous CTD casts were made to characterize the evolving soliton field at the moored array site located in approximately 75 m of water. The orientation of the local isobaths at this site is 50° T.

Rank-ordered groups of solitons with four or five constituent members traveled by the site approximately every 12.4 hours. Phase speeds were shown to have a mean of 61.8 ± 14.9 cm/s, and were sometimes in excess of 100 cm/s. The rank-ordered groups traveled across the shelf with an average heading of 280 ± 31° T. The average maximum vertical displacement of the solitons was 4.8 ± 3.3 m with the largest displacement recorded being 20 m. Within each group, rank-ordering appropriately described both phase speed and displacement characteristics. The only exception to these facts was during a strong wind event which effectively switched off the generation mechanism near the end of the experiment. During that time period, soliton groups were almost completely absent.

Although the ocean exhibited stratification throughout the water column, the predictions of two-layer finite-depth theory seem adequate to describe some key features associated with the solitons. They appear as waves of depression, with maximum displacements at the effective layer interface. Their heading is orthogonal to the local bathymetry and shows good agreement with previous remote sensing results - a good confirmation of the T-string antenna technique. The horizontal velocity field changes sign in the center of the pycnocline, and the vertical structure of the horizontal velocity field shows nearly 90% of the total variance in the first baroclinic mode. For one soliton group examined in detail, the observed phase speed increased with increasing maximum vertical displacement, and the rate of increase is predicted by finite-depth theory. The magnitude of the phase speed is overpredicted by finite-depth theory, presumably due mainly to the effects of continuous stratification. The decrease in characteristic horizontal scale with increasing maximum displacement is also captured by finite-depth theory.

The limitations of this data set are clear. A more complete explanation of the soliton field could be provided by in-situ high-frequency measurements of parameters other than temperature. Most importantly, quality measurements of the salinity field at the same location as the T-string antenna would have eliminated the need to use CTD data to provide a proxy for the density field. Also, the more members in an antenna the more precise the measurements of heading and phase speed. In SWARM, although five T-strings were deployed, only three worked well enough to be used as a soliton antenna.

References

Apel, J.R., Byrne, M., Proni, J.R., and Charnell, R.L., Observation of Oceanic Internal and Surface Waves From the Earth Resources Technology Satellite, *Journal of Geophysical Research, 80,* 865- 881, 1975a.

Apel, J. R., Proni J. R., Byrne, H. M., and Sellers, R. L., Near-simultaneous Observations of Intermittent Internal Waves on the Continental Shelf from Ship and Spacecraft, *Geophysical Research Letters, 2,* 128, 1975b.

Baines, P.G., The Generation of Internal Tides by Flat-Bump Topography, *Deep Sea Research, 20,* 179-205, 1973.

Baines, P.G., The Generation of Internal Tides Over Steep Continuous Slopes, *Phil. Trans. Roy. Soc. London, 277,* 27-58, 1974.

Baines, P.G., On Internal Tide Generation Models, *Deep Sea Research, 29,* 307-338, 1982

Benjamin, T.B., Internal Waves of Finite Amplitude and Permanent Form, *Journal of Fluid Mechanics, 25,* 241-270, 1966.

Benjamin, T.B., Internal Waves of Permanent Form in Fluids of Great Depths, *Journal of Fluid Mechanics, 29,* 559-592, 1967.

Benney, D.J., Long Nonlinear Waves in Fluid Flows, *J. Math. and Phys., 45,* 52-63, 1966.

Defant, A., *Physical Oceanography, 2,* Pergamon, 1961.

Djordjevic, V.D. and Redekopp, L.G., The Fission and Disintegration of Internal Solitary Waves Moving over Two-Dimensional Topography, *Journal of Physical Oceanography, 8,* 1016-1024, 1978.

Ekman, V.W., 1904, On Dead Water, Scientific Results. Norway. North Polar Expedition. 5, 15, 1893-1896.

Hibiya, T., Generation of Internal Waves by Flow Over a Sill, *Journal of Geophysical Research, 91,* 7697-7708, 1986.

Hibiya, T., Generation Mechanism of Internal Waves by Tidal Flow Over Stellwagen Bank, *Journal of Geophysical Research, 93,* 533-542, 1988.

Joseph, R.I., Solitary Waves in a Finite Depth Fluid, *J. Phys. A: Math. Gen., 10,* L225-l227, 1977.

Korteweg, D.J. and de Vries, G., On the Change of Form of Long Waves Advancing in a Rectangular Canal, and on a new Type of Long Stationary Waves, *Phil Mag., 39,* 422, 1895.

Kubota, T., Ko, D.R.S., and Dobbs, L., Propagation of Weakly Nonlinear Internal Waves in a Stratified Fluid of Finite Depth, *J. Hydronautics, 12,* 157-165, 1978.

Marsden, R.F., The Internal Tide on Georges Bank, *Journal of Marine Research, 44,* 35-50, 1986.

Moody, J. A., Butman, B., Beardsley, R. C., Brown, W., Daifuku, P., Irish, J. D., Mayer, D. A., Mofjeld, H. O., Petrie, B., Ramp, S., Smith, P., and Wright, W. R., *Atlas of Tidal Elevation and Current Observations on The Northeast American Continental Shelf and Slope,* USGS Bulletin 1611, 1984.

Ono, H., Algebraic Solitary Waves in Stratified Fluids, *J. Phys. Soc. Japan, 39,* 1082-1091, 1975.

Osborne, A.R., and Burch, T.L., Internal Solitons in the Andaman Sea, *Science, 208,* 451-460, 1980.

Osborne, A. R., Burch, T. L., and Scarlet, R. I., The Influence of Internal Waves on Deep Water Drilling, *Journal of Petroleum Technology, 30,* 1497, 1978.

Phillips, O. M., *The Dynamics of the Upper Ocean,* Cambridge University Press, Cambridge, 1966.

Russell, J.S., Report on Committee on Waves, *Report of the Seventh Meeting of British Association of Science,* London, John Murray, 417-496, 1838.

Wallinga, J.P., On the Internal Semidiurnal Tide in Stellwagen Basin, University of New Hampshire, M.S. Thesis, 1995.

Zabusky, N.J. and Kruskal, M. D., Interaction of "Solitons" in a Collisionless Plasma and the Recurrence of Internal States. *Phys. Rev. Lett., 15,* 240, 1965.

Zheng, Q., Yan, X.H., and V. Klemas, Statistical and Dynamical Analysis of Internal Waves on the Continental Shelf of the Middle Atlantic Bight from Space Shuttle Photographs, *Journal of Geophysical Research, 98,* 8495 - 8504, 1993.

Appendix A

Soliton field time series

High-pass filtered time series of temperature for each of the thermistor strings used in the antenna are presented. Note the approximately 12-hour spacing of the soliton envelopes as well as the smaller abundance toward the end of the period. The wind event of August 7 (yearday 219) shows up in these records as a relative lack of solitons and no discernable phase locked energy bursts.

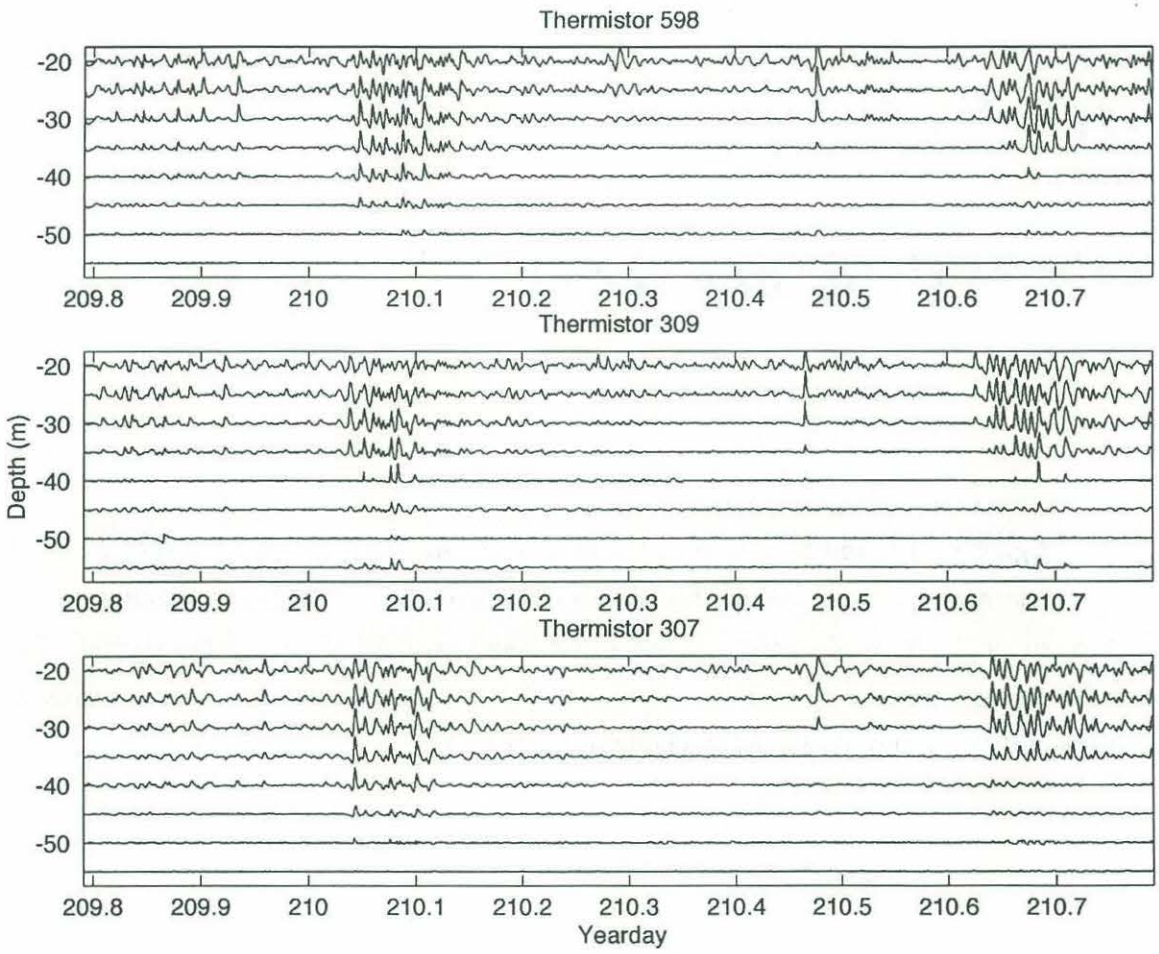
Thermistor 598
-20
-30
-40
-50
209.8
209.9
210
210.1
210.2
210.3
210.4
210.5
210.6
210.7
Thermistor 309
Depth (m)
Thermistor 307
Yearday

Figure A1

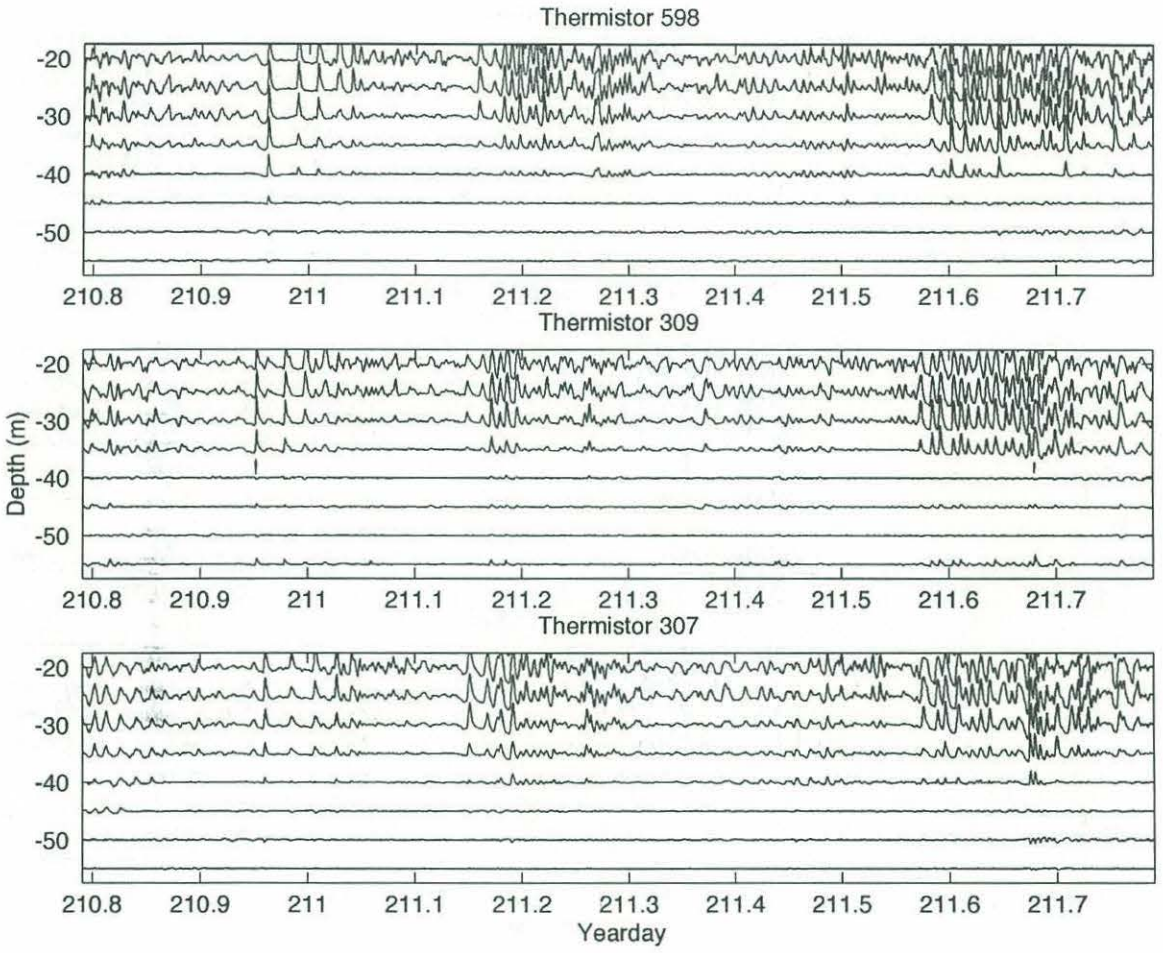

Figure A1: continued

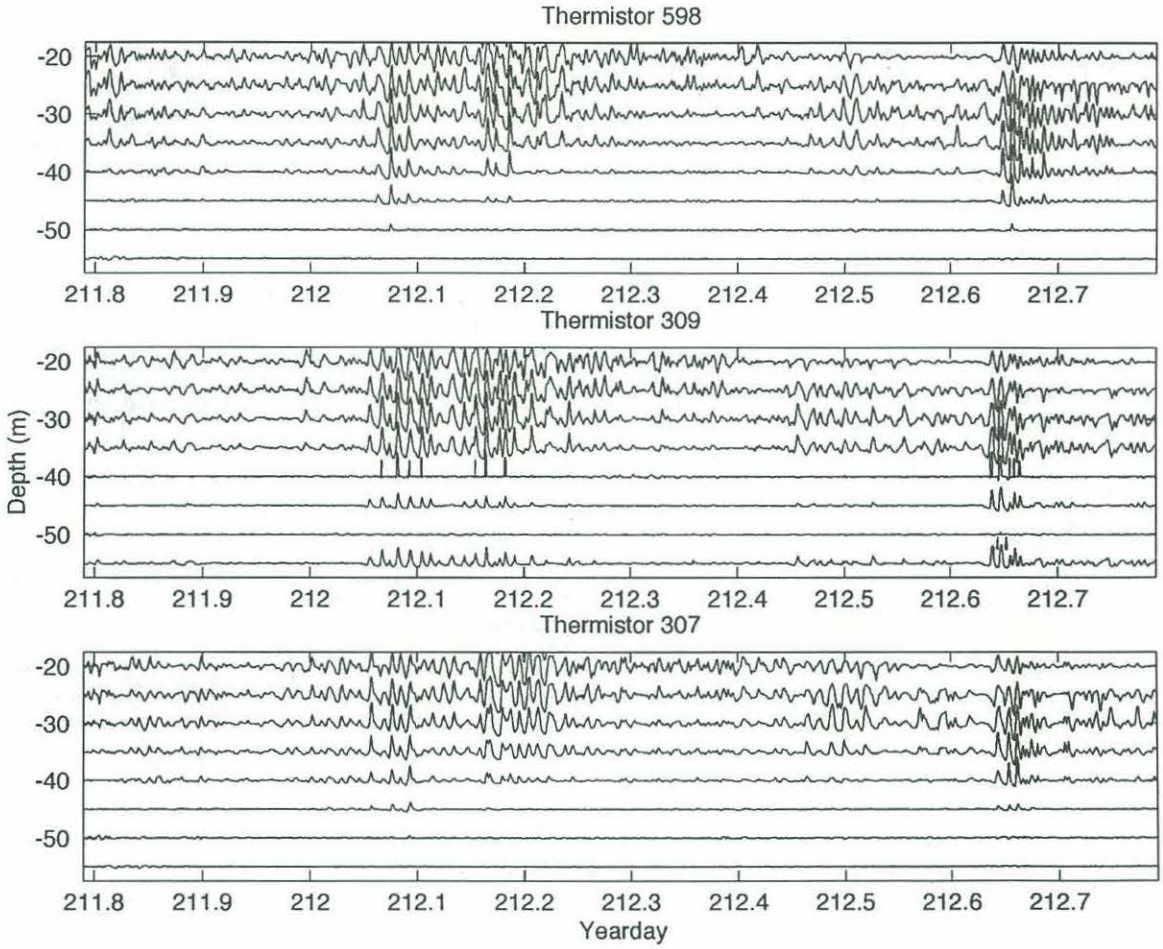

Figure A1: continued

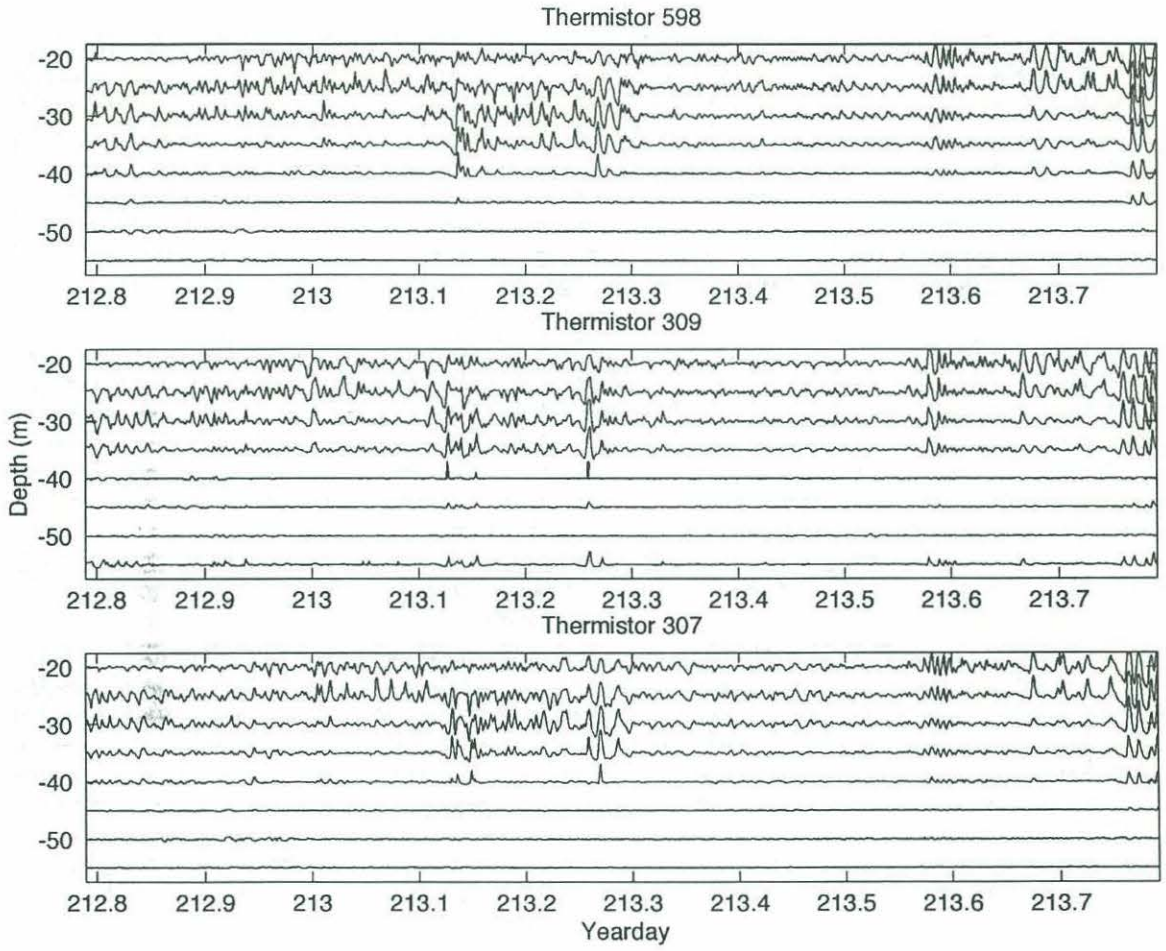

Figure A1: continued

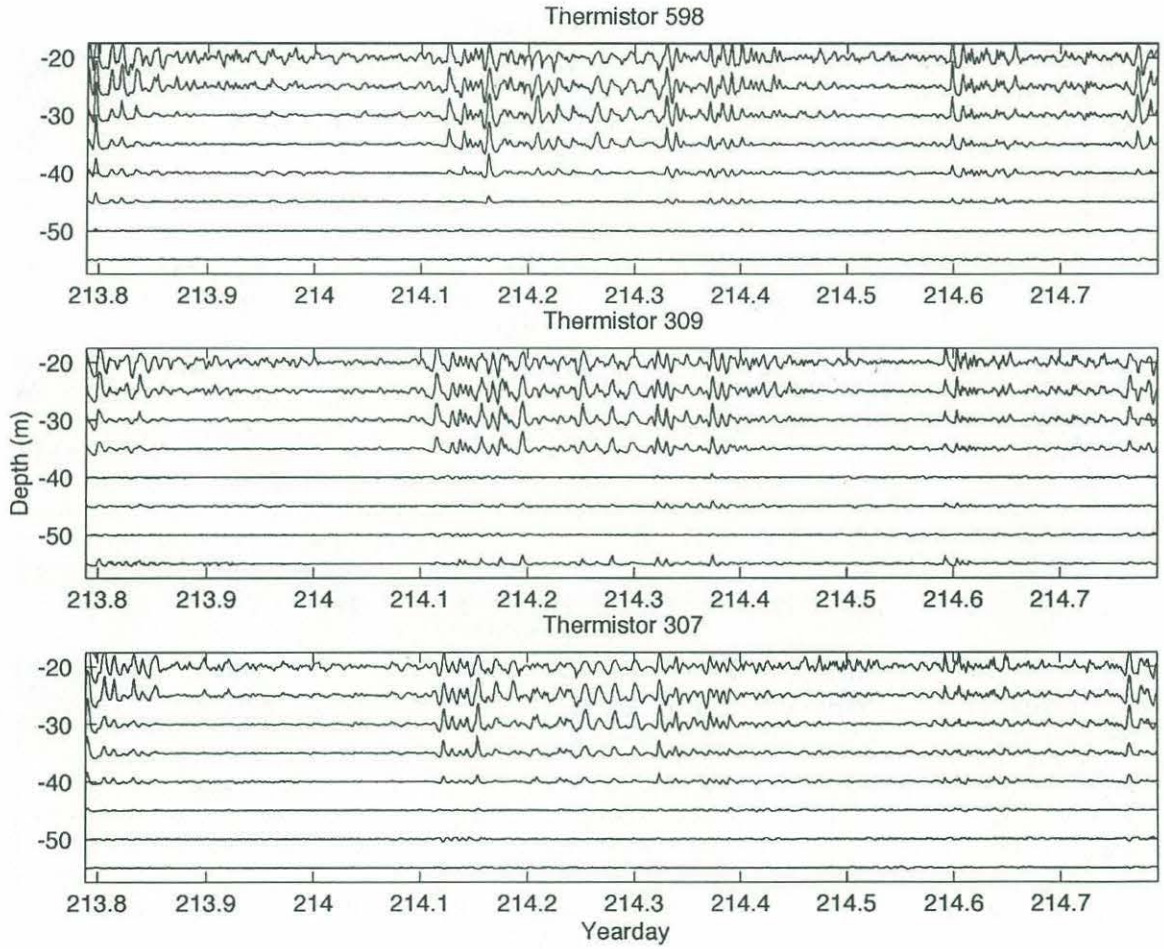

Figure A1: continued

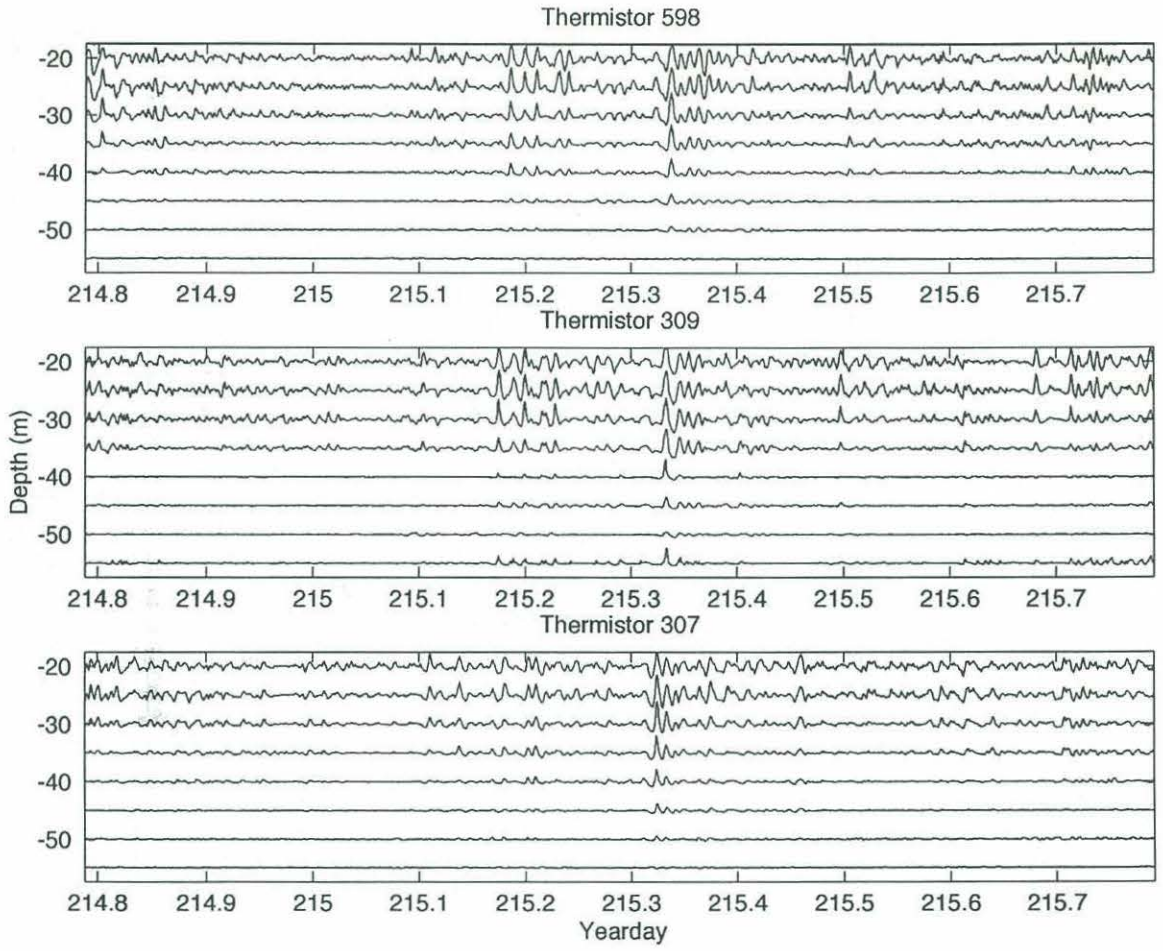

Figure A1: continued

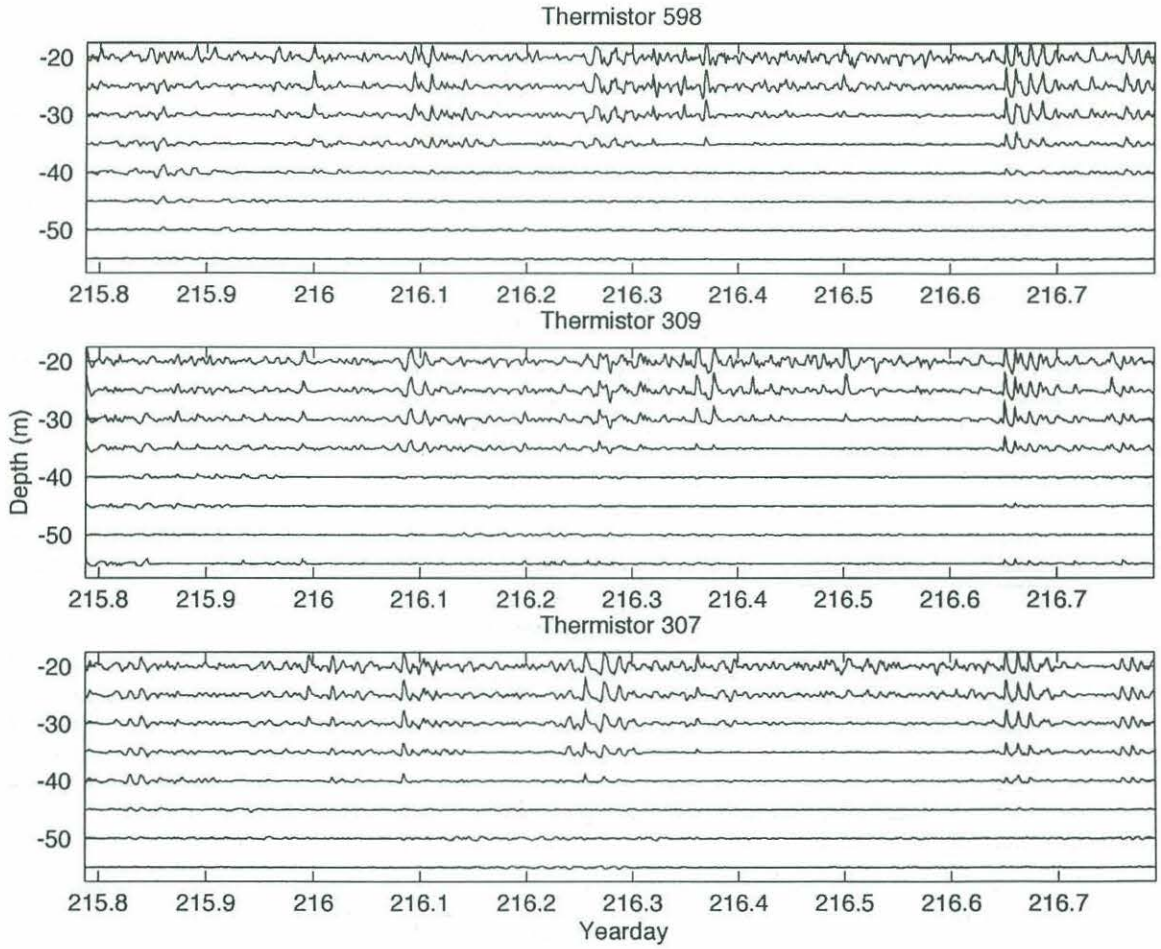

Figure A1: continued

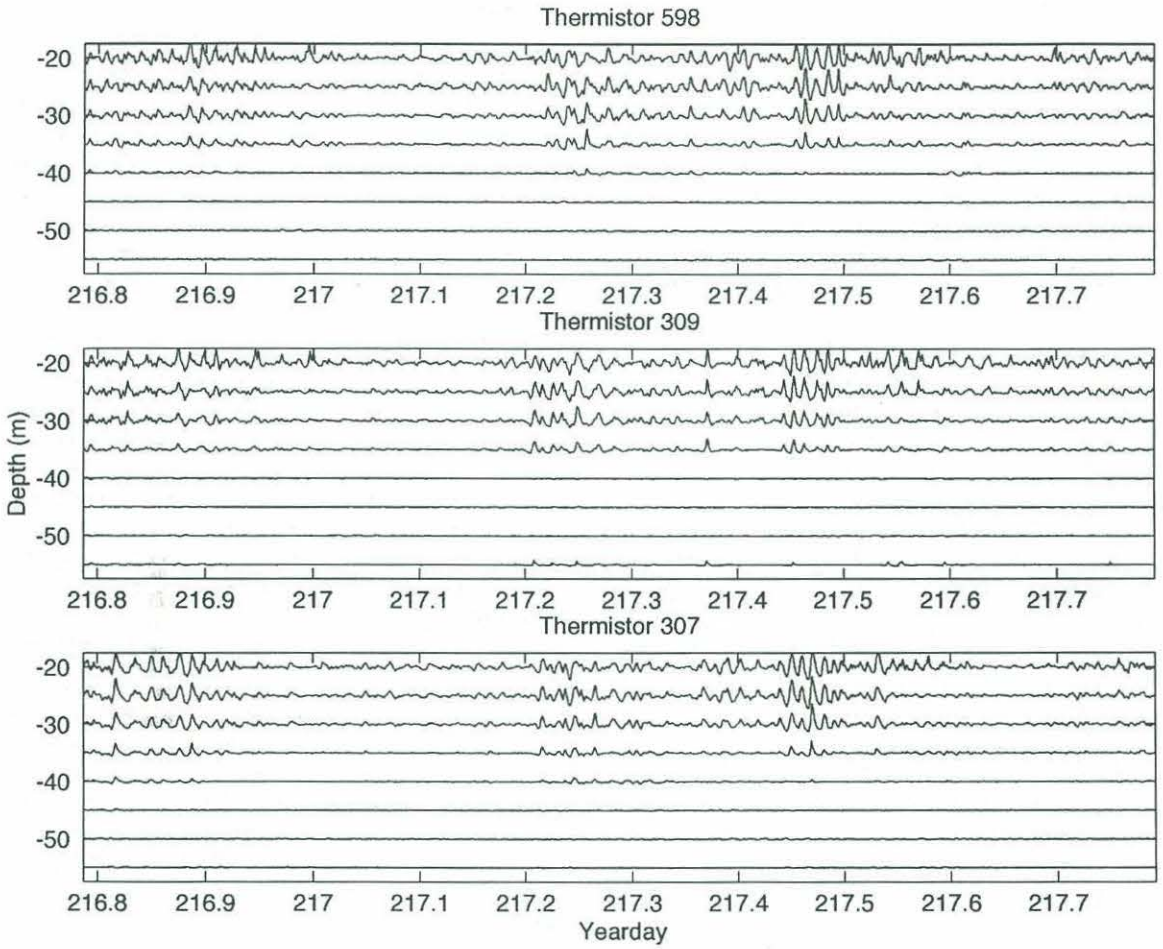

Figure A1: continued

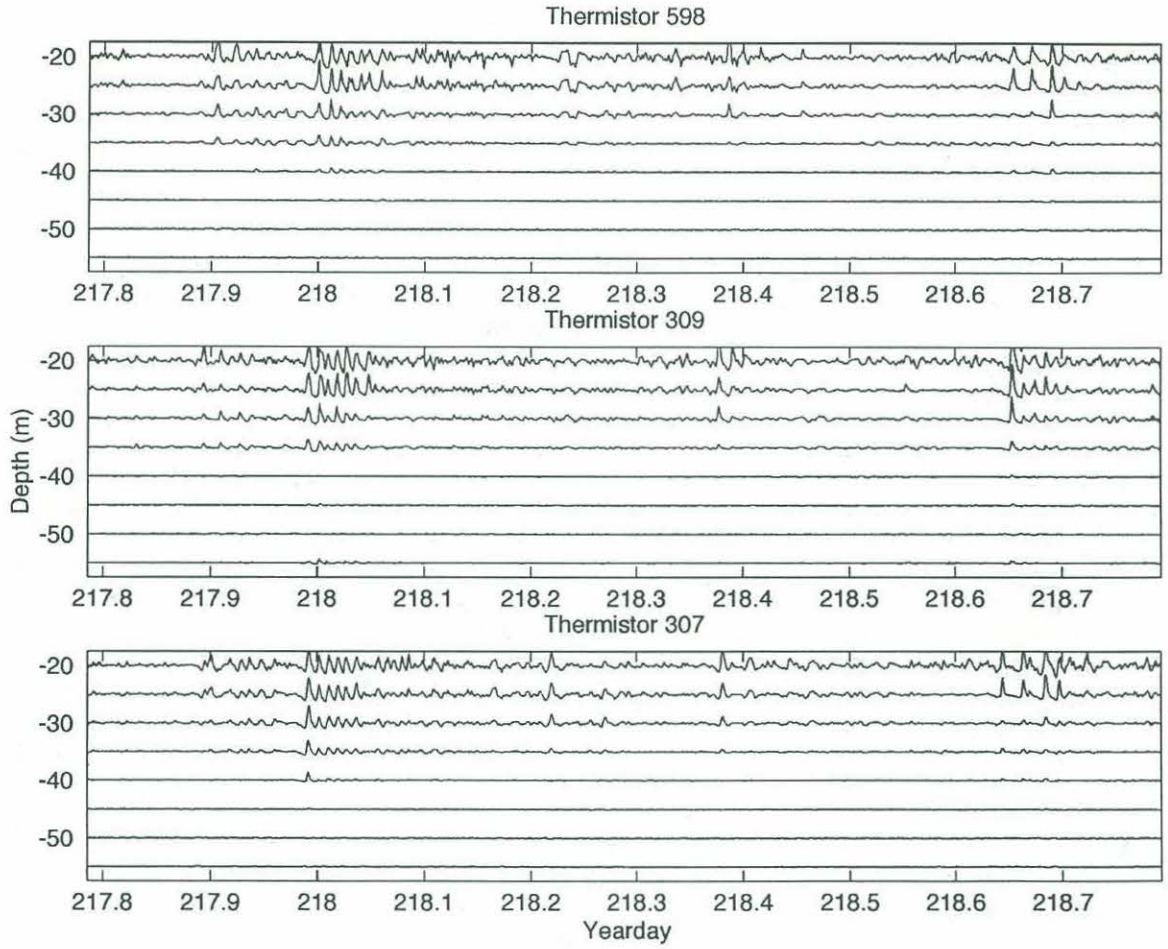

Figure A1: continued

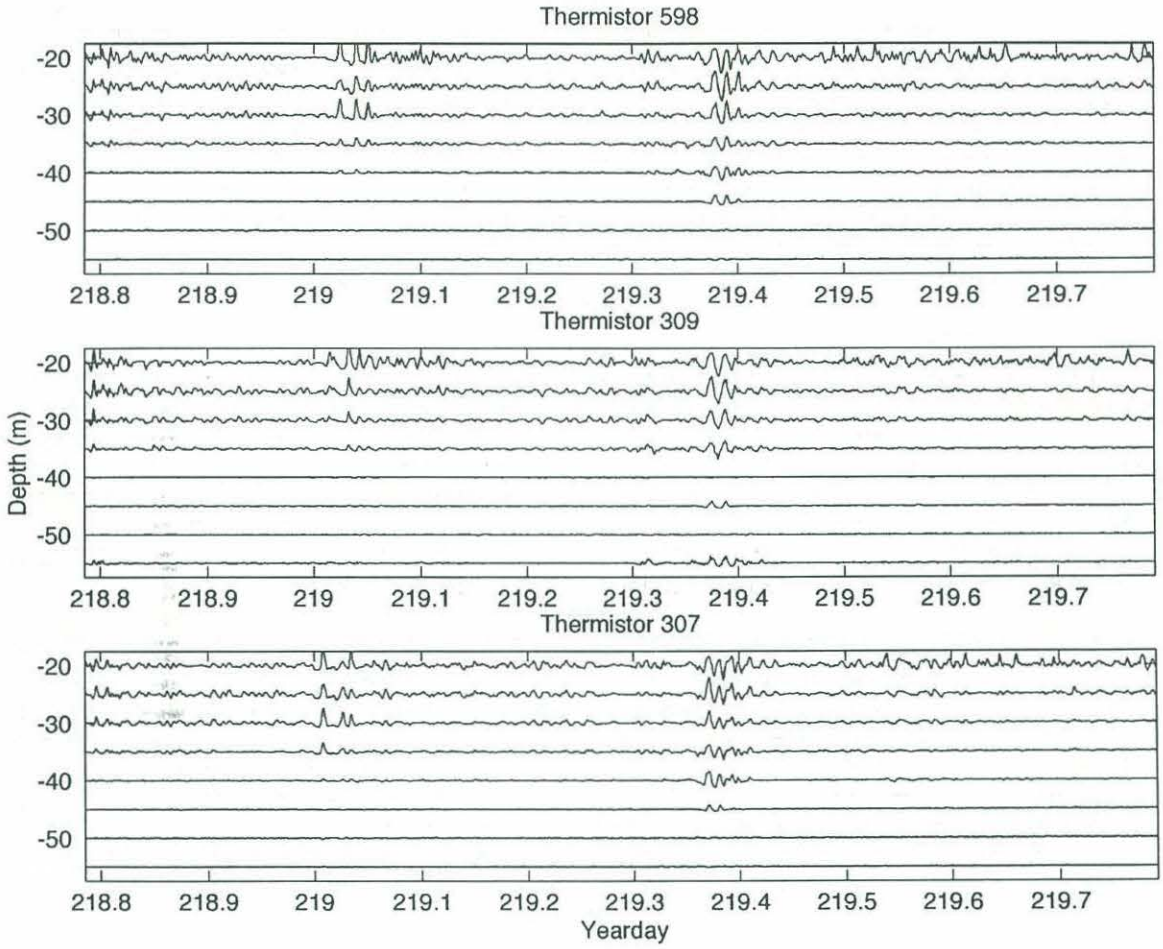

Figure A1: continued

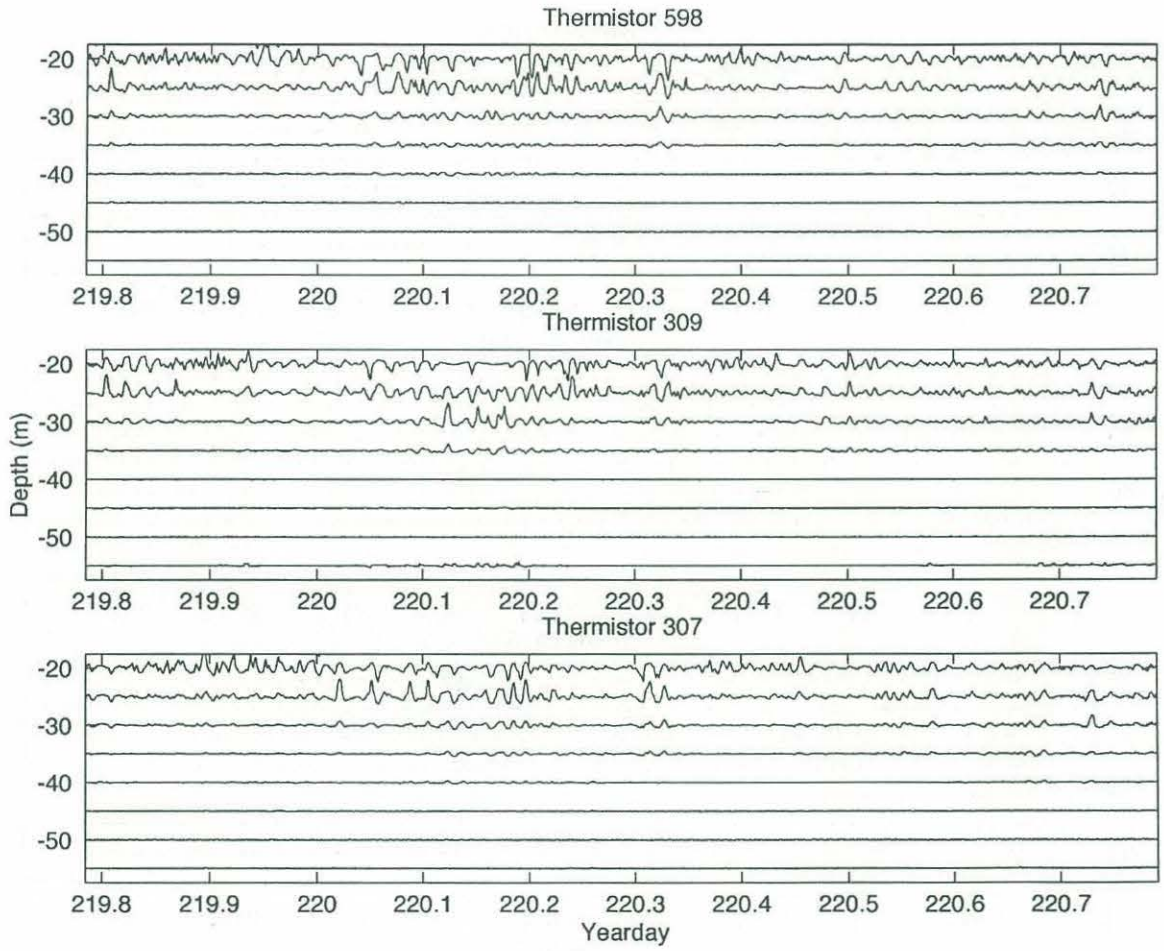

Figure A1: continued

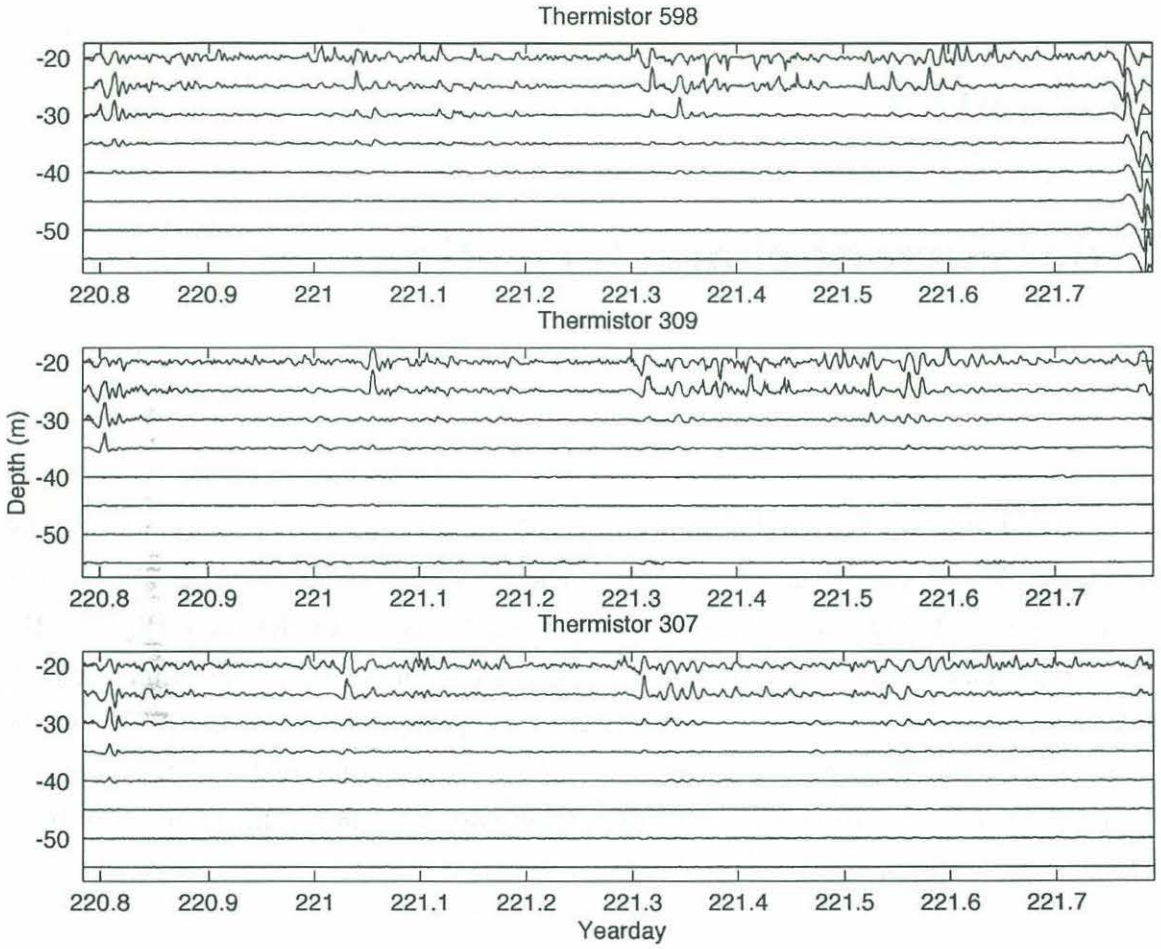

Figure A1: continued

Appendix B

Tidal current characterization

The following four sets of figures depict the tidal currents in a variety of ways for depths 23, 35, 47, and 59 m respectively. The upper left hand corner is a plot of u versus v for the low-passed time series and as such traces out the tidal ellipse. The upper right hand corner is a time series of the angle from north that the tidal vector is pointing as a function of time - note the lack of complete rotation for the period of the large wind event. The lower left hand corner is a feather plot of the velocity vector, again clearly showing the storm's influence at these depths. Finally, the lower right hand corner shows a compass histogram of angular direction.

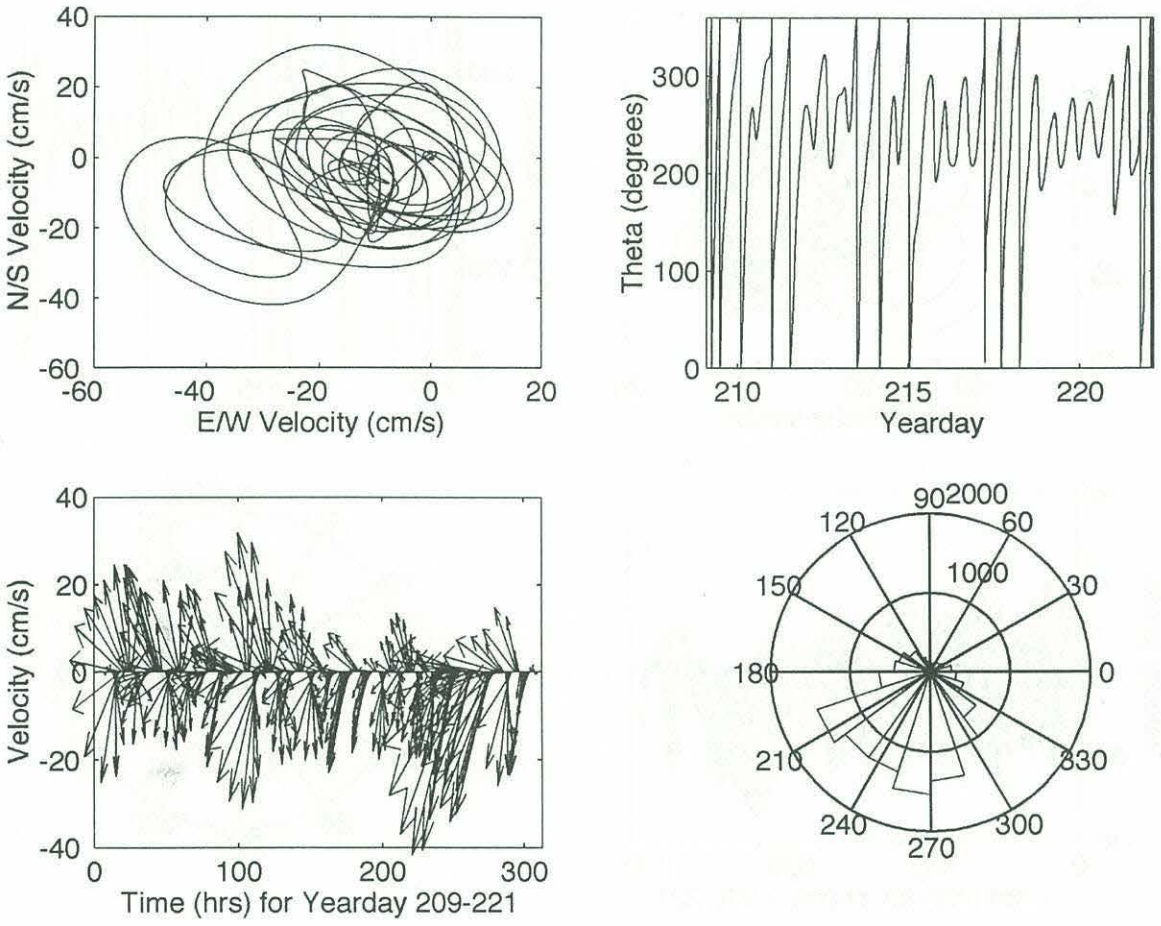

Figure B1: Depth = 23 m.

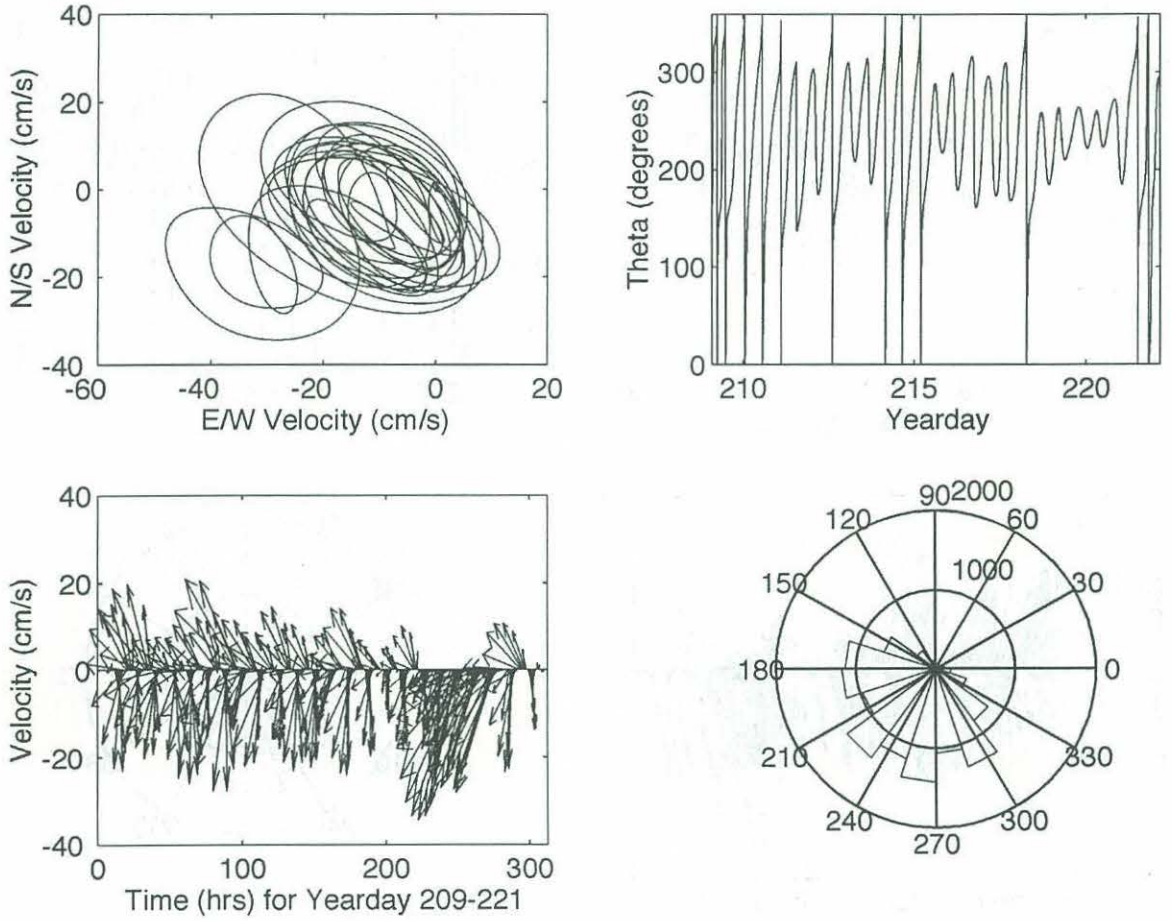

Figure B2: Depth = 35 m.

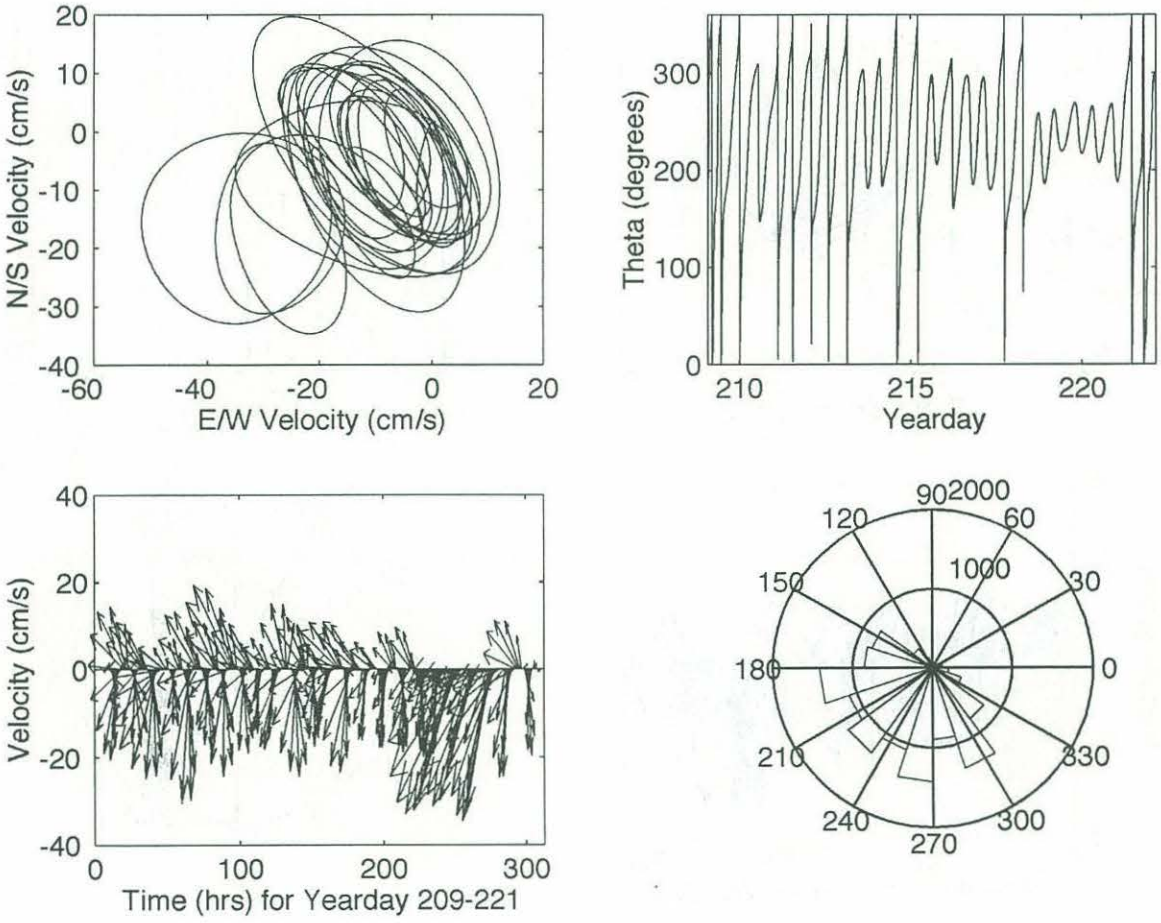

Figure B3: Depth = 47 m.

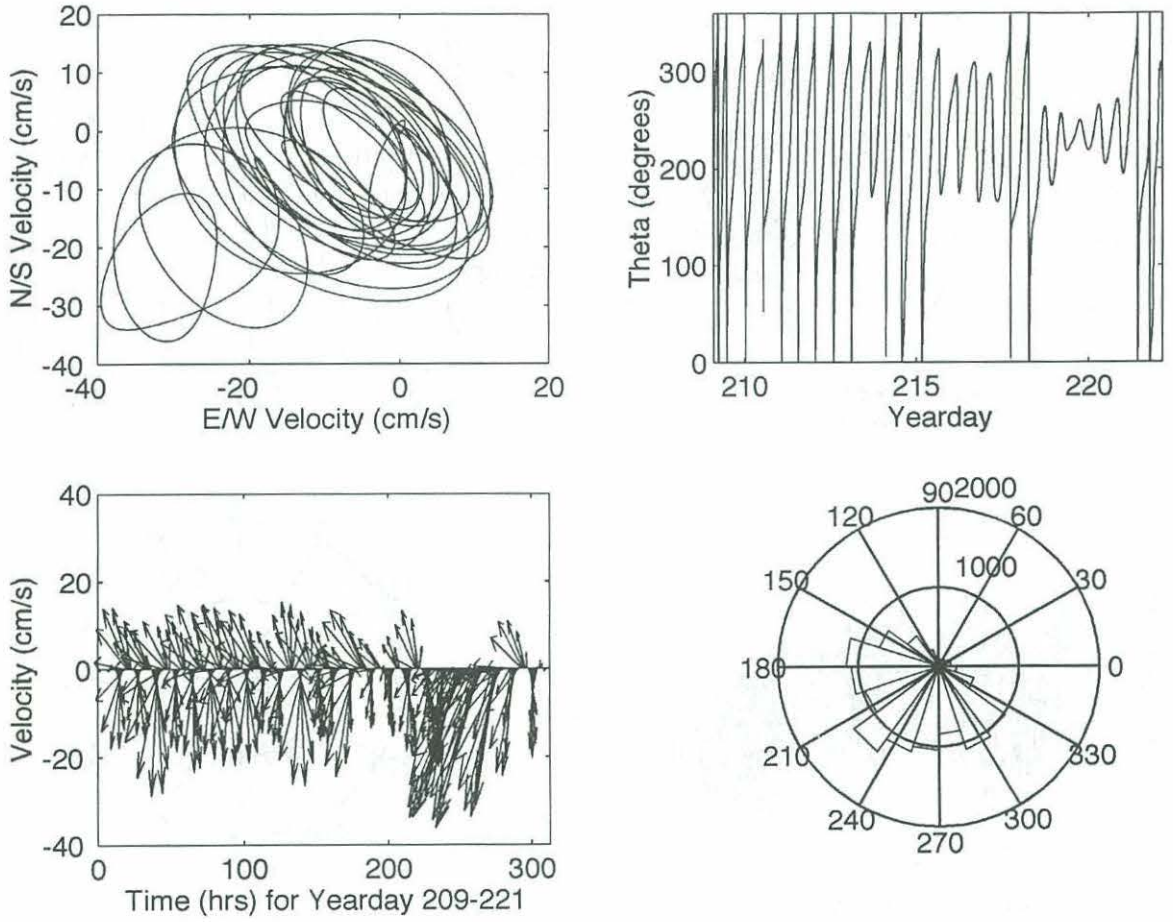

Figure B4: Depth = 59 m.

Appendix C

Heading histograms for solitons

This appendix contains histograms of the soliton headings for each depth that the analysis was executed for. This ranges from 67 - 7 m depth. Note the change in direction from offshore to onshore as we move from the deeper into the shallower water. This is due to the fact that particle velocities are opposite to the direction of phase propagation in the lower layer. Although included here, the 7-m and 11-m depth bins were not used due to side-lobe contamination of the ADCP current data.

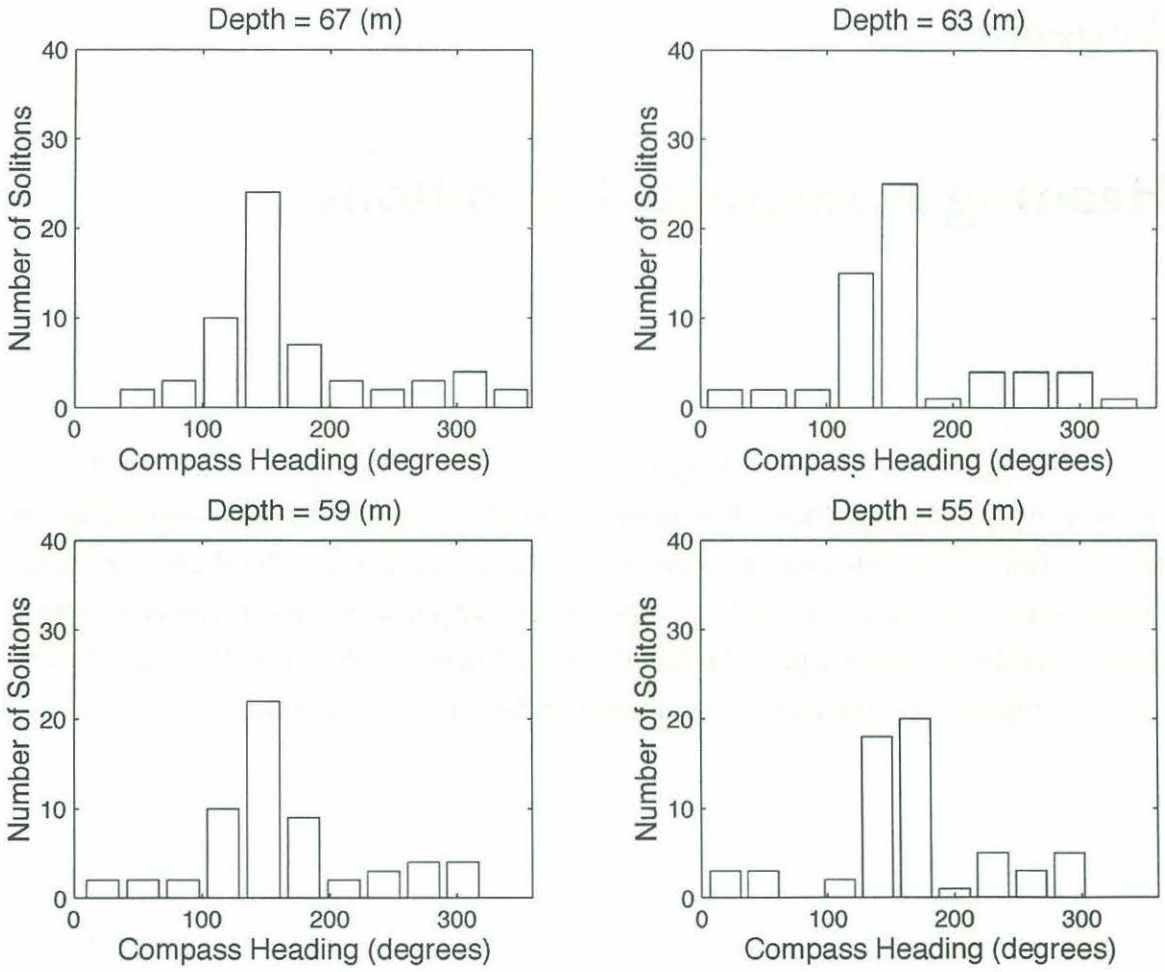

Figure C1: Depths 67 - 55 m.

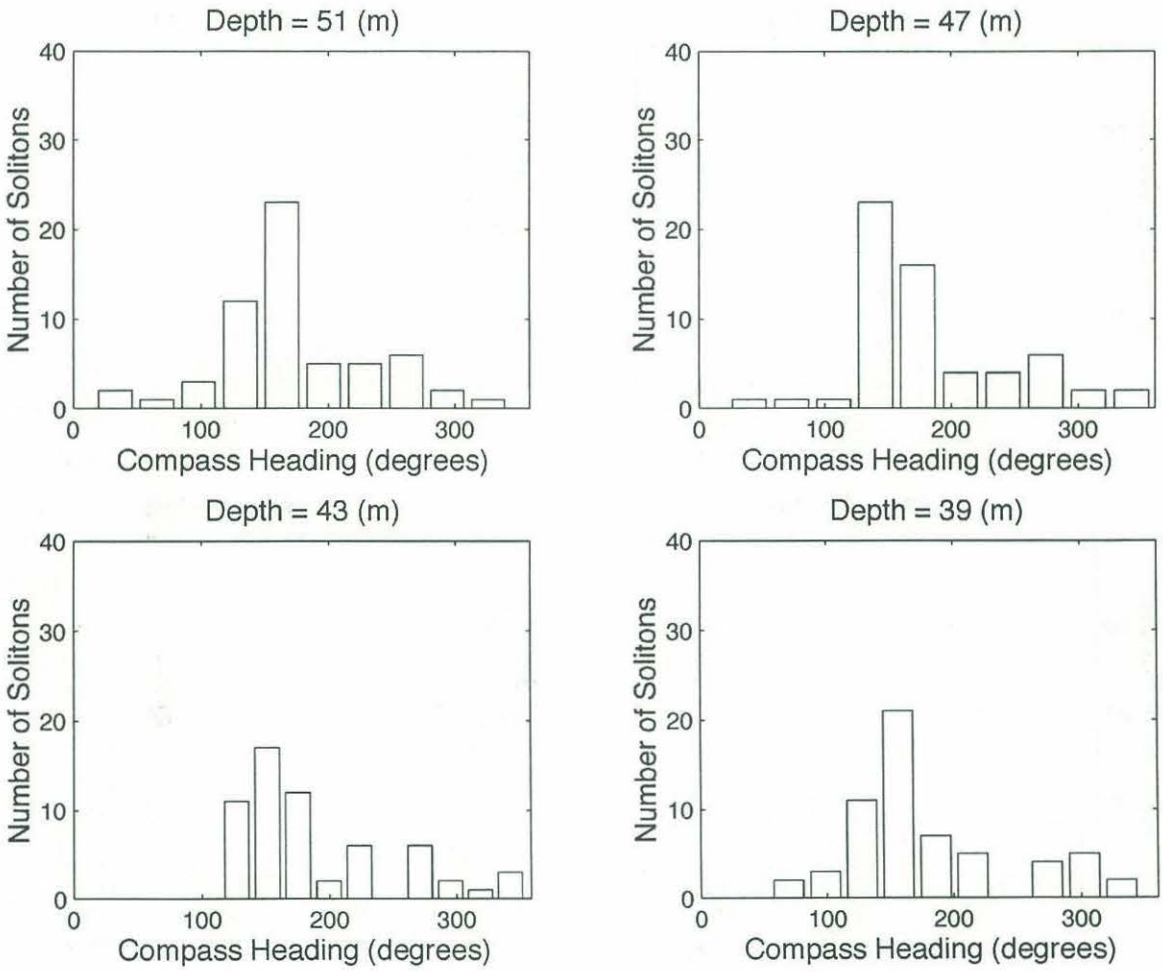

Figure C2: Depths 51 - 39 m.

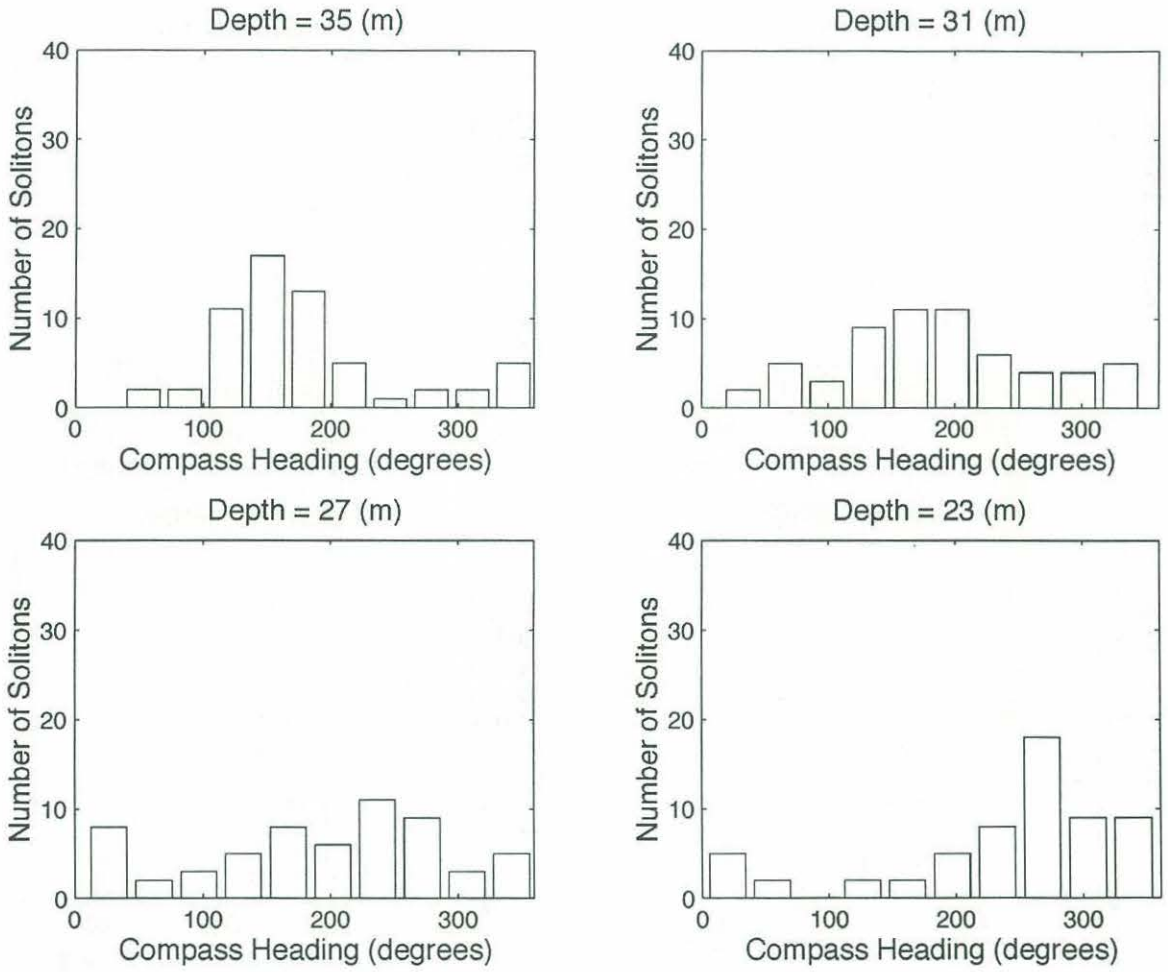

Figure C3: Depths 35 - 23 m.

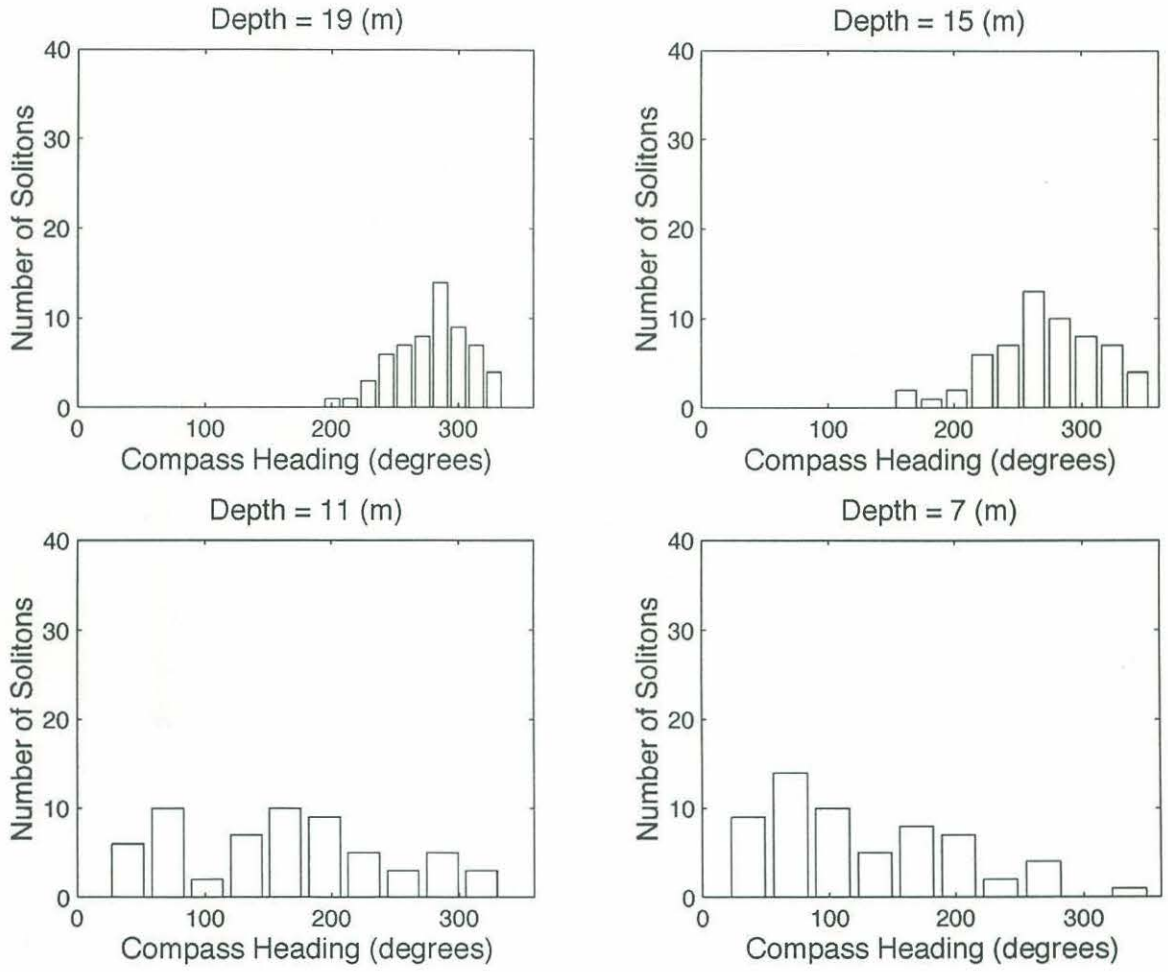

Figure C4: Depths 19 - 7 m.